# Computational optimization of the piston bowl geometry for the different combustion regimes of the dual-mode dual-fuel (DMDF) concept through an improved genetic algorithm

Energy Conversion and Management
Volume 246, 15 October 2021, 114658
https://doi.org/10.1016/j.enconman.2021.114658

Guangfu Xu [a], Antonio García [b], Ming Jia [a, *], Javier Monsalve-Serrano [b]

[a] Key Laboratory of Ocean Energy Utilization and Energy Conservation of Ministry of Education, Dalian University of Technology, Dalian, 116024, P.R. China

[b] CMT - Motores Térmicos, Universitat Politècnica de València, Camino de Vera s/n, 46022 Valencia, Spain

* Corresponding author:

Ming Jia

School of Energy and Power Engineering

Dalian University of Technology

Dalian, 116024

P.R. China

**Tel:** +86-411-84706722

**Fax:** +86-411-84706722

**Email:** jiaming@dlut.edu.cn

# Computational optimization of the piston bowl geometry for the different combustion regimes of the dual-mode dual-fuel (DMDF) concept through an improved genetic algorithm

Guangfu Xu [a], Antonio García [b], Ming Jia [a,*], Javier Monsalve-Serrano [b]

[a] Key Laboratory of Ocean Energy Utilization and Energy Conservation of Ministry of Education, Dalian University of Technology, Dalian, 116024, P.R. China

[b] CMT - Motores Térmicos, Universitat Politècnica de València, Camino de Vera s/n, 46022 Valencia, Spain

## Abstract

Focusing on the dual-mode dual-fuel (DMDF) combustion concept, a combined optimization of the piston bowl geometry with the fuel injection strategy was conducted at various loads. An improved genetic algorithm was introduced in this study, which is superior in searching for the global optimal solutions. The optimal piston bowl shape coupled with the corresponding injection strategy was summarized at the various loads. The results show that the piston bowl geometry optimization can further improve the thermal efficiency with 1.4%, 4.4%, and 1.4% percentage points for the low, mid, and high loads, respectively. An indicated thermal efficiency up to 51.8% can be realized at mid load. Meanwhile, for all the optimal cases, $NO_x$ and soot emissions can meet the Euro VI limits.

At low and mid loads, both the open and re-entrant type piston bowl can be equipped, while the high load only prefers the open type piston bowl for the DMDF mode. The re-entrant type or deep piston bowls are superior in organizing strong in-cylinder flow, which is beneficial for the fuel/air mixing. The open type or shallow piston bowls are helpful for reducing the heat transfer losses owing to the less heat transfer surface area. Furthermore, a correlation analysis was conducted to investigate the sensitivity of engine performance to the piston geometric parameters and

injection parameters. It is concluded that the fuel injection event becomes more important for managing the engine performance as load increases. Among the injection parameters, the influence of the fuel injection timings and injection pressure on engine performance is more obvious. The piston geometric parameters play more significant roles in the heat transfer losses than the injection parameters for all loads. Among the geometric parameters, the most influential parameters are the width and open extent of the piston bowl. The heat transfer loss energy fraction can be well decreased with a wider and more open piston bowl.

**Keywords**: Piston bowl geometry optimization; Dual-mode dual-fuel (DMDF); Genetic algorithm; Fuel efficiency; Correlation analysis

## Graphical abstract

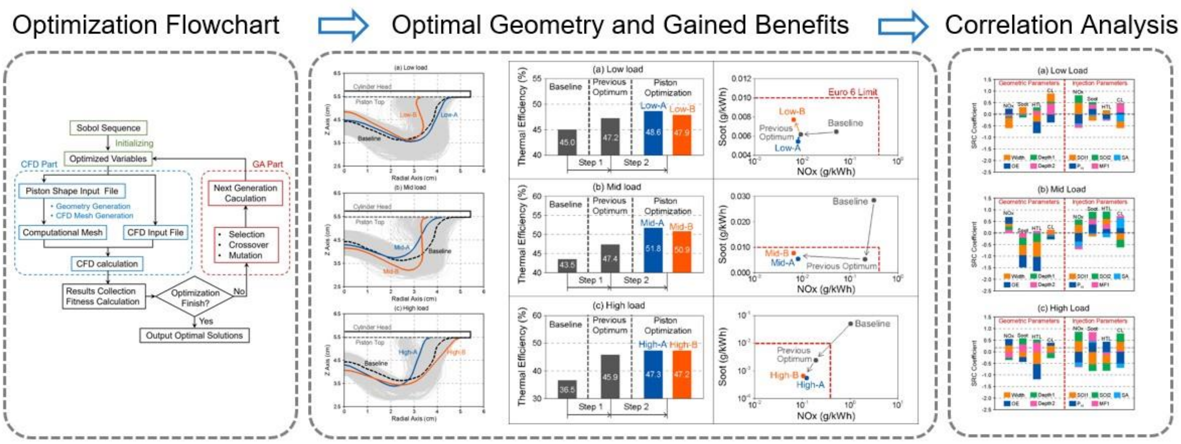

**Nomenclature**

| | |
|---|---|
| 1D | one-dimensional |
| 3D | three-dimension |
| ATDC | after top dead center |
| CA50 | 50% burn point |
| CDC | conventional diesel combustion |
| CFD | computational fluid dynamics |
| CL | combustion losses |
| CO | carbon monoxide |
| DI | direct injection |
| DMDF | dual-mode dual-fuel |
| DOE | design of experiment |
| DPF | diesel particulate filter |
| EGR | exhaust gas recirculation |
| EISFC | equivalent indicated specific fuel consumption |
| EPA | Environmental Protection Agency |
| GA | genetic algorithm |
| GCR | geometric compression ratio |
| HRR | heat release rate |
| HC | hydrocarbon |
| HCCI | homogeneous charge compression ignition |
| HTL | heat transfer losses |
| HTR | heat transfer rate |
| ICE | internal combustion engine |
| IMEP | indicated mean effective pressure |
| ISFC | indicated specific fuel consumption |
| IVC | intake valve closing |
| LHV | lower heating value |
| LTC | low-temperature combustion |
| MF1 | mass fraction of the first injection |
| NSGA | non-dominated sorting genetic algorithm |
| $NO_x$ | nitrogen oxides |
| OE | Open Extent |
| $p_{inj}$ | injection pressure |
| $p_{ivc}$ | inital pressure at IVC timing |
| $p_{max}$ | maximum in-cylinder pressure |
| PPC | partially premixed combustion |
| PPRR | peak pressure rise rate |
| PR | premix ratio |
| RCCI | reactivity controlled compression ignition |
| RI | ringing intensity |
| SA | spray angle |
| SCR | selective catalytic reduction |
| SOI | start of injection |
| SOI1 | start of injection timing for first pulse |
| SOI2 | start of injection timing for second pulse |
| SRC | Spearman Rank Correlation |
| TDC | top dead center |
| $T_{ivc}$ | initial temperature at IVC timing |
| VVT | variable valve timing |

# 1. Introduction

The increasingly stringent emission regulations and urgent energy shortage are bringing huge challenges for the internal combustion engine (ICE) research community. Improving fuel economy and eliminating engine-out emissions are still the major objectives and main investigation fields for ICE researchers. Currently, the selective catalyst reduction (SCR) and diesel particulate filter (DPF) systems have been widely adopted by engine manufacturers as the aftertreatment devices for decreasing nitrogen oxides ($NO_x$) and soot emissions, respectively. Although their effectiveness has been demonstrated, the engine layout complexity and cost are increased as well [1]. Alternatively, the low-temperature combustion (LTC) strategy [2] was proposed, which yields great potential of reducing $NO_x$ and soot emissions while maintaining pleasant fuel economy owing to the characteristics of homogeneous-mixing and low-temperature combustion process.

Among the LTC modes, reactivity controlled compression ignition (RCCI) [3] concept attracts more scientific interest due to the flexible control over the combustion process with the dual-fuel system. In RCCI mode, the fuel concentration and reactivity stratification can be accomplished relying on delivering the low-reactivity fuel by port fuel injection (PFI) and the high-reactivity fuel by in-cylinder direct injection (DI), respectively. By adjusting the low-reactivity fuel percentage and the direct injection event, the fuel distribution and reactivity can be tuned, and a flexible operation in a wide operating range can be realized [4]. In spite of this, the RCCI strategy is still facing the problems of low combustion efficiency at low load [5, 6] and serious engine noise at high load [7]. Thus, the improvement of the RCCI strategy over a wide operating range is still needed.

Up to now, many investigations focus on the extension of the RCCI operation range. Lim et al. [8] found that extremely low $NO_x$ and soot emissions, as well as the indicated thermal efficiency of 48.7% can be reached for a gasoline/diesel RCCI engine at high load up to 21 bar of the indicated mean effective pressure (IMEP). Wang et al. [9] demonstrated the effectiveness of exhaust gas recirculation (EGR) rate for preventing excessively high peak pressure rise rate (PPRR) and extending the RCCI mode to higher loads. Meanwhile, it was found that the employment of gasoline/diesel dual-fuel RCCI mode at mid and high loads can maintain ultra-low $NO_x$ and soot emissions, while the diesel LTC strategy with single fuel injection is more attractive for low load conditions.

Molina et al. [10] extended the RCCI operating range by employing a multiple direct-injection strategy combined with the Miller cycle. At low load, the double injection strategy was used for managing the combustion phasing and emissions. At high load, the injection shifts into a single injection for triggering the ignition and maintaining mild combustion. Xu et al. [11, 12] optimized the key parameters of an RCCI engine couple with the the variable valve timing (VVT) and variable compression ratio (VCR) strategies at various load conditions. The results indicated that the Euro VI limit can be well maintained over the whole load range, whereas the trade-off of the $NO_x$ and soot emissions at high load is difficult to solve. Mikulski et al. [13] found that early intake valve closing is beneficial for the RCCI operation at high load, whereas retarding the intake valve opening timing can reduce combustion losses.

Benajes et al. [14] indicated that 80% of the nominal operating range for conventional diesel engines can be covered by the RCCI operation by employing appropriate fuel ratio, EGR rate, and intake temperature, while the PPRR limit will not be surpassed. Based on that study, a dual-mode dual-fuel (DMDF) concept was proposed by Benajes et al. [15]. In the DMDF concept, the combustion mode was shifted regarding the engine load. At low load, the highly-premixed RCCI operation was employed for enhancing the engine efficiency and obtaining low levels of emissions. At high load, the combustion mode was switched to diffusive combustion for slowing down the combustion rate and meeting the engine mechanical restriction. Recently, a series of efforts were made for the development of the DMDF concept, as summarized in Table 1.

Table. 1. A Summary of the main papers published on DMDF combustion mode

| Reference | Contents of the research | Main Conclusions |
|---|---|---|
| Benajes et al. | The DMDF concept was proposed featuring | • The DMDF concept can fulfill the EURO |

| | | |
|---|---|---|
| [15] (2017) | that the combustion strategy changes as engine load increases.<br>• At low loads with the indicated mean effective pressure (IMEP) lower than 8 bar, a fully premixed RCCI strategy is employed;<br>• When engine load rises up to 15 bar, the combustion strategy is switched to highly premixed RCCI mode;<br>• At full load operation, the diffusive dual-fuel combustion is employed. | VI $NO_x$ limit up to 14 bar IMEP;<br>• Above 5 bar IMEP, the smoke emissions exceed the EURO VI standards for diesel engines, but the majority of the engine map can fulfill the smoke levels below 1 FSN. |
| Benajes et al. [16] (2018) | Comparison of the performance and emissions of two dual-mode combustion concepts over different driving cycles using different fuel combinations. | The dual-mode concept has a potential to be implemented in flexible-fuel engines. |
| García et al. [17] (2019) | Investigation of the effects of the octane number of the low-reactivity fuel at representative operating conditions over the DMDF engine map. | The characteristics of the low-reactivity fuel in the DMDF concept have a major impact on the combustion evolution in a wide range of engine load, speed, low-reactivity fuel fraction, dilution level, and combustion regime. |
| Macián et al. [18] (2019) | Investigation of the effect of the low-pressure exhaust gas recirculation (LP-EGR) on the gaseous and particle emissions of the DMDF concept fueled with standard gasoline and diesel. | • In the fully premixed RCCI mode, the application of the LP-EGR results in high hydrocarbon (HC) and carbon monoxide (CO) emissions;<br>• For the other combustion modes in the DMDF concept, a reduction of the analyzed pollutants is demonstrated with the employment of the LP-EGR compared with the CDC mode. |
| Xu et al. [19] (2020) | Optimization of the operating parameters related to the intake condition and fuel injection strategy for strengthening the engine performance of the DMDF concept fueled with gasoline and diesel fuel at various load conditions. | Gross indicated thermal efficiency above 45% is achieved, and the $NO_x$ and soot emission can be maintained under the Euro VI standard for the whole load range. |
| García et al. [20] (2020) | Exploring the feasibility of using the fuel blend of oxymethylene ether ($OME_x$) and diesel as the high-reactivity fuel instead of pure diesel in the DMDF concept for reducing the | The $OME_x$-diesel blends with an $OME_x$ mass content greater than 70% are able to meet the Euro VI $NO_x$ standard with ultra-low soot levels (< 0.01 g/kWh) up to 80% engine load. |

| | | |
|---|---|---|
| | lifecycle $CO_2$ emission. | |
| García et al. [21] (2020) | Exploration of suitable injector configuration and fuel injection strategy for the DMDF concept with diesel and $OME_x$ respectively as the high-reactivity fuels. | • The long injection durations of $OME_x$ resulted from its low lower heating value is handled with the employment of the injectors with higher flow rate capacity.<br>• The trade-off relationship between engine-out emissions and the mixing capacity of the injection system is solved, while the engine performance is not significantly affected. |

Up to date, the DMDF strategy demonstrates superior advantages for balancing load extension and performance improvement. It has been recognized as a promising dual-fuel combustion concept to satisfy future fuel consumption and emission regulations [17]. However, for the current DMDF strategy, there still exist some aspects to be further improved, among which the piston bowl geometry optimization is the most urgent. At present, the piston bowl geometry for the DMDF strategy is empirically determined. It is well known that the piston bowl geometry can exert significant influences on engine performance. Moreover, the interactions between the piston bowl structure and the injection event are crucial for the fuel/air mixture formation and combustion event for the dual-fuel combustion mode. Thus, the combined optimization of the piston bowl shape with the fuel injection parameters is needed to further enhance the DMDF combustion characteristics.

Up to now, many investigations have been conducted for studying the effects of the piston bowl geometry and searching for the optimal bowl shape for the engines with advanced combustion concepts. Dempsey et al. [22] compared the traditional re-entrant type with a modified shallow type piston based on an RCCI engine fueled with different fuel combinations. It was concluded that the shallow type piston yields better engine efficiency due to lower heat transfer losses. Similar results were also reported by Park et al. [23] that the shallow type piston bowl can contribute to a 35% improvement of the gross indicated thermal efficiency. Xu et al. [24] performed an investigation to study the joint effects of the bowl shape and injection timing based on the partially premixed combustion (PPC) mode and homogeneous charge compression ignition (HCCI) mode. The results indicated that the piston with a stepped-lip shape is favorable for solving the low-load cold start problem in terms of decreasing the intake temperature requirement, which is owing to the fact that the fuel-rich regions can be produced in the stepped-lip piston bowl. Moreover, it was found that the effect of spray/wall interaction is important when the combustion mode shifts from HCCI to PPC. Nazemian et al. [25] optimized the piston bowl geometry of an RCCI engine by utilizing CONVERGE software combined with the design of experiment (DOE) method based on the second law of thermodynamics, and the effects of the main piston bowl shape parameters, including the piston bowl sizes, pip height, and top land height on exergy destruction were discussed. It was reported that the influence of the bowl diameter and bowl depth were the most significant of the exhaust heat recovery. The optimization study performed by Lee et al. [26] indicated that a 9% improvement of fuel consumption with simultaneously reduced $NO_x$ and soot emissions can be attained with a shallow type piston bowl and a narrow injection angle for a gasoline/diesel dual-fuel engine.

From the above literature review, it is confirmed that further optimization of the piston bowl shape used for the DMDF strategy can lead to potential improvements in fuel efficiency and engine-out emissions. Moreover, up to date, there have been few studies reporting the piston bowl geometry optimization over a wide load range for the engines with advanced combustion modes. Thus, in this study, the combined optimization of the piston bowl shape parameters with the fuel injection strategy was conducted over a wide load range for the DMDF mode based on an improved genetic algorithm integrated with the computational fluid dynamics (CFD) simulation. Then, the optimal piston bowl shape coupled with the injection strategy was summarized at different loads. Furthermore, a correlation analysis was conducted to investigate the sensitivity of engine performance to the geometric parameters and injection parameters, which can guide the engine structure design.

# 2. Computational Method

## 2.1. Generation of the Piston bowl geometry and computational mesh

In this study, the shape of the piston bowl is generally described using two straight lines (*i.e.*, Line 1 and Line 2) and three circle curves (*i.e.*, Curve 1, Curve 2, and Curve 3) according to the work of Badra et al. [27]. The straight lines and circle curves are represented by the blue and red lines respectively in Fig. 1. It is comprehensible that the shape is determined by the location of circles A, B, and C, as well as their common tangent lines. Thus, the controllable parameters contain the *X* and *Z* locations of the circle center points A, B, and C, as well as the radius of the three circles, *i.e.*, $R_a$, $R_b$, and $R_c$. Compared with the traditional method, in which the piston bowl shape is described by the Bezier Curve, the control variables are simplified, and the variable number is cut down to seven with this method. In general, once the coordinates and the radius of the three circles are confirmed, the angles of $\alpha$ and $\theta$ (see Fig. 1) can be determined. Thus, the point number and the coordinates of every single point on the piston bowl shape line can be determined, and the piston bowl geometry can be described.

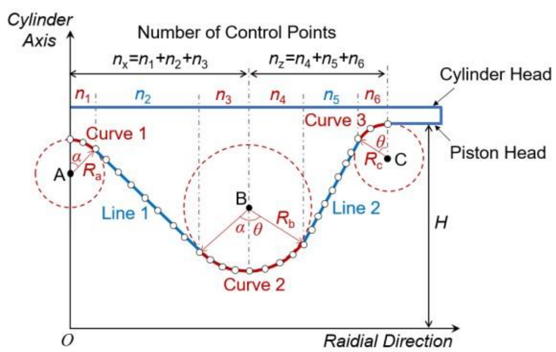


Fig. 1. Illustration of automatic generation of the piston bowl geometry.

The common piston bowl geometries widely used in previous studies for advanced combustion modes, including the Open, Re-entrant, and Shallow piston bowl geometries, can be established using this method, as shown in Fig. 2. Because the bowl shape is specifically determined by the size and location relationship of the three control circles, it can be flexibly controlled by the variables shown in Fig. 1 for the optimization of the bowl shape. Fig. 3 illustrates the computational mesh generation process. In this study, the computational mesh is generated using the pre-processing tool for mesh establishment in the KIVA code. The input file for the pre-processing program is integrated with the geometry generation code according to the shape input file, which includes the information of the three control circles (*i.e.*, circles A, B, and C). Among various generated meshes, the computational sector meshes of three typical piston bowl geometries with the geometric compression ratio of 14.4 are shown in Fig. 2. It can be seen that the computational sector meshes for the Open, Re-entrant, and Shallow piston bowls can be well generated.

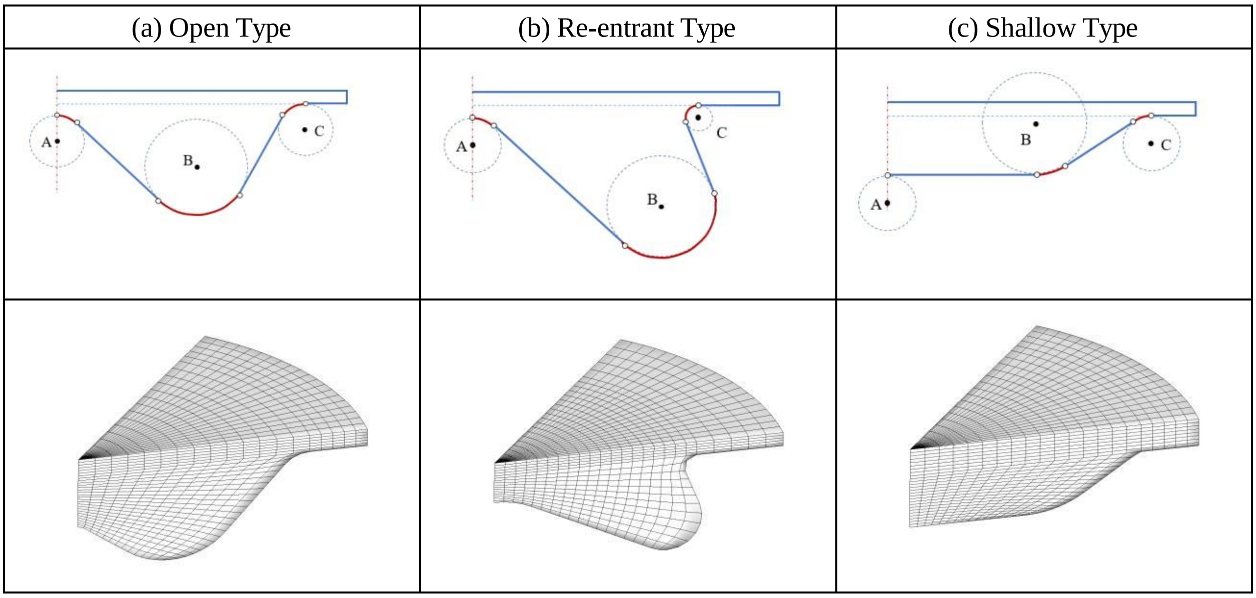


Fig. 2. Common piston bowl types and corresponding computational meshes at top dead center.

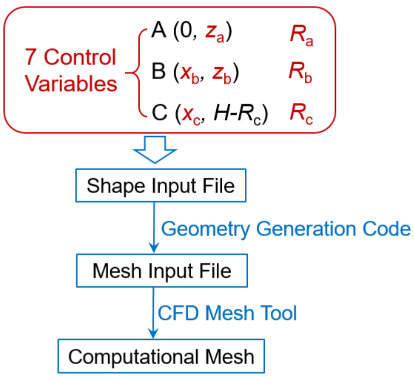


Fig. 3. Computational mesh generation procedure.

## 2.2. CFD Model

The CFD calculation of this study was conducted using the open-source KIVA-3V code [28] for simulating the engine working process. Based on the framework of KIVA-3V, several improvements and updates about the sub-models have been performed. The turbulence model improved by Wang et al. [29] was used for modeling the in-cylinder flow. The improved models were used for modeling the spray impingement [30] and liquid film evolution processes [31]. Moreover, the quasi-dimensional model for describing the vaporization processes of fuel droplets [32] and liquid films [33] was integrated. Meanwhile, the wall heat transfer model [34], droplet collision model [35], and droplet breakup model [36] were also contained in this CFD code. For dealing with the fuel chemistry, the KIVA-3V code was coupled with the CHEMKIN solver [37]. Furthermore, the skeletal chemical mechanism constructed by Chang et al. [38] was used for predicting the ignition and combustion characteristics of the fuel blends. The diesel and gasoline fuel were represented by *n*-heptane and *iso*-octane, respectively. It should be noted that the above models have been validated based on numerous experimental data in the previous works, e.g., Refs. [39, 40].

Table 2. Engine specifications

| | |
|---|---|
| Bore (mm) | 110.0 |
| Stroke (mm) | 135.0 |
| Connecting rod length (mm) | 212.5 |
| Original compression ratio | 14.4:1 |
| Swirl Ratio | 2.3 |
| Direct fuel injection system | Common rail |
| Number of nozzle holes | 7 |
| Spray angle (°) | 75.0 |
| Nozzle hole diameter (mm) | 0.177 |

The computational model was validated ahead of the optimization study. Table 2 lists the detailed information of the engine tested in this work. The validation was performed at a constant engine speed of 1200 rev/min with different IMEP. Table 3 lists the basic conditions and the operating parameters of the validation cases. Table 4 lists the the properties of the diesel and gasoline fuels tested in the experiment [15]. Fig. 4 illustrates the computational mesh for the original DMDF combustion chamber, and the mesh is generated using the method mentioned above. Fig. 5 illustrates the comparison of the simulated and experimental in-cylinder pressure and heat release rate (HRR) traces for five test cases with different IMEP. The comparison results show that the simulated traces can well match with the measurements of Benajes et al. [15]. This indicates that the simulation with the generated computational mesh can accurately reproduce the combustion process of the DMDF mode at different loads.

Table 3. Basic conditions of the validation cases.

| IMEP (bar) | 5.9 | 9.9 | 11.9 | 17.3 | 22.6 |
|---|---|---|---|---|---|
| $p_{ivc}$ (bar) | 1.60 | 2.29 | 2.32 | 3.01 | 3.09 |
| $T_{ivc}$ (K) | 332.6 | 329.1 | 347.9 | 332.2 | 356.1 |
| EGR rate (%) | 19.7 | 55.5 | 50.2 | 45.1 | 31.0 |
| SOI1 (°CAATDC) | -48.0 | -50.0 | -45.0 | - | - |
| SOI2 (°CAATDC) | -41.9 | -4.4 | -5.0 | 0.0 | 6.0 |
| Total fuel flow (mg/cycle) | 35.5 | 65.2 | 81.1 | 116.9 | 145.3 |
| Diesel flow (mg/cycle) | 31.8 | 62.3 | 50.4 | 52.9 | 49.3 |
| Gasoline flow (mg/cycle) | 3.7 | 2.9 | 30.7 | 64.0 | 96.0 |

Table 4. Properties of the diesel and gasoline fuels

| | Diesel | Gasoline |
|---|---|---|
| Density (kg/m$^3$) @ T=288.15 K | 824 | 720 |
| Viscosity (mm$^2$/s) @ T=313.15 K | 2.8 | - |
| Research Octane Number (-) | - | 95 |
| Motor Octane Number (-) | - | 85 |
| Cetane Number (-) | 51 | - |
| Lower Heating Value (kJ/kg) | 42.92 | 42.40 |

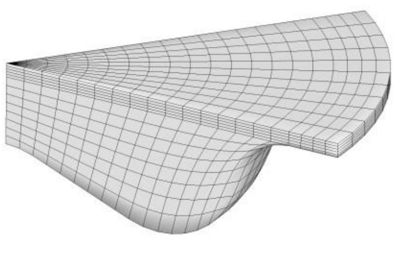

Fig. 4. Computational mesh for the original DMDF combustion chamber.

Fig. 6 shows comparisons of HC, CO, $NO_x$ and soot emissions between simulation and experiment. It is found that the overall variation trend with varying IMEP can be well captured for the four emissions. However, the discrepancies in magnitude still exist between the simulated and experimental emission levels. This is primarily owing to the complexity of the in-cylinder flow and fuel/air mixing process, the imperfection of the chemical mechanism [41], and the measurement uncertainties [3]. Since the main task of the simulation tool of this study can be qualified by the capability of predicting the emission variation trend as a specific operating parameter changes, the computational model and mesh can be employed for the optimization study in the following work.

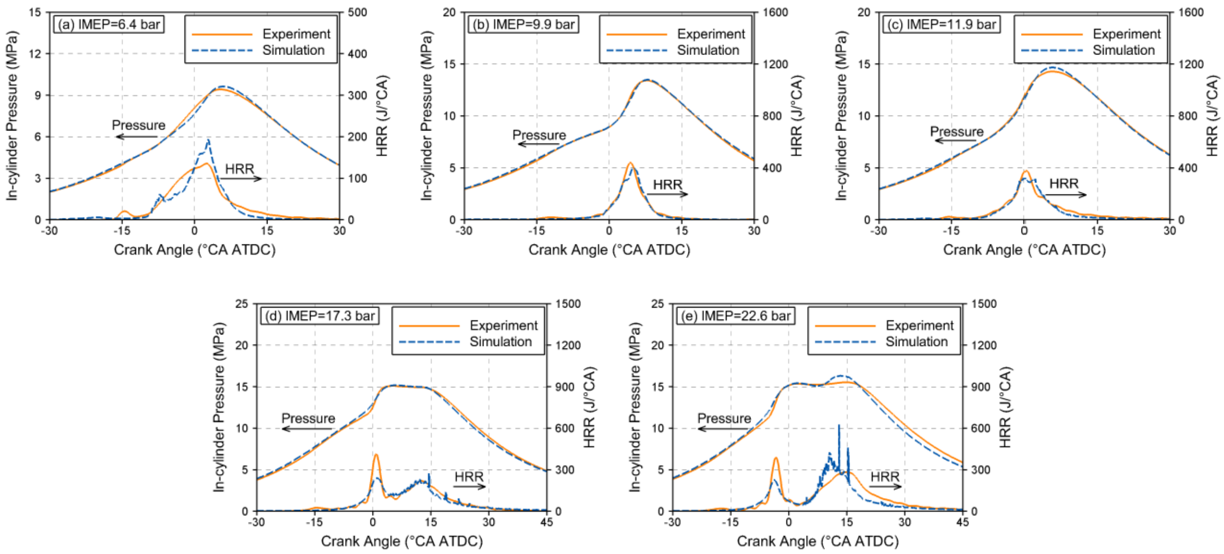


Fig. 5. Validations of the pressure and HRR at different loads.

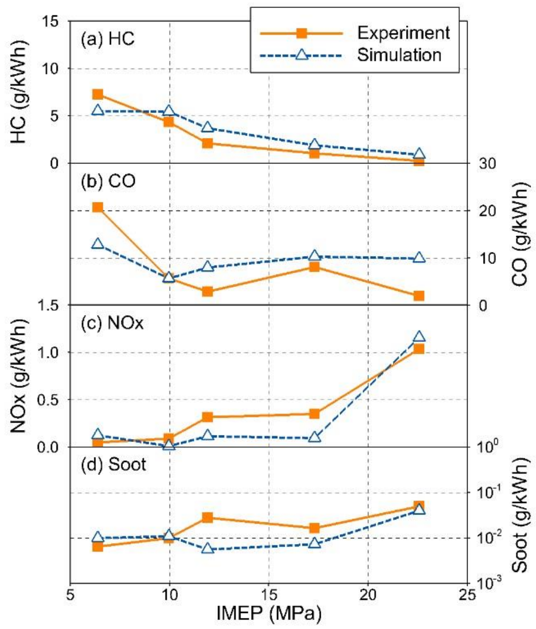


Fig. 6. Validations of the emissions at different loads.

## 2.3. Optimization method

In this study, the optimization of the piston bowl geometry coupled with the injection strategy involves a considerable number of variables. In order to realize the multi-variable multi-objective optimization and simultaneously minimize the fuel consumption and engine-out emissions, the non-dominated sorting genetic algorithm II (NSGA-II) [42] was utilized. The flowchart of the optimization procedure is illustrated in Fig. 7. The global numerical system contains two parts, *i.e.*, the optimization part using GA and the CFD part using KIVA. The GA code is coupled with the KIVA code containing the geometry generation code. In the optimization calculation, the GA code generates the shape input and CFD input files. The geometry generation code is in charge of exporting the mesh input file, which is the input file for the meshing program to create the computational mesh. CFD calculation is performed with the CFD input file and the computational mesh. GA code analyzes the CFD calculation results of each citizen and generates new data for the next generation calculation.

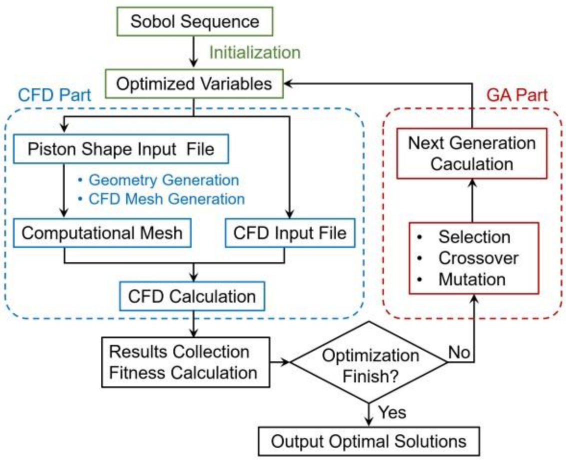


Fig. 7. Illustration of the optimization computation process.

Considering the increased number of variables, the initial population size needs to be enlarged to keep the diversity of the optimal solutions in the GA calculation. In this study, the initialization of the citizens for the first generation is improved by introducing the Sobol sequence sampling method [43] instead of the traditional random sampling method used in NSGA-II. Fig. 8 shows the distributions of the random samples and Sobol samples with a constant sample number of 250 in a two-dimensional variable coordinate. It can be found that the distribution of the Sobol samples is more uniform than that of the random samples. This indicates that the Sobol sequence sampling method can provide a better uniformity for the multi-dimensional variables by sufficiently covering the whole variation ranges of the variables under the conditions with limited population size. Therefore, the introduction of the Sobol sequence sampling method in this study is aiming at including more possible cases and searching for the global optimal solutions more effectively, and a relatively small population size can be utilized simultaneously for saving computational resources.

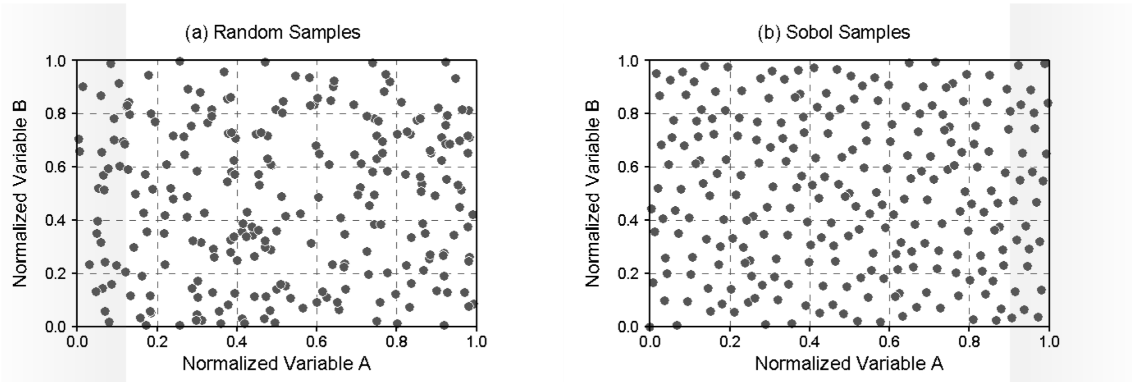


Fig. 8. Comparison of random samples and Sobol samples.

# 3. Results and Discussion

## 3.1. Global optimization results

In a previous study from the authors [19], based on the diesel/gasoline DMDF combustion concept, the operating parameters related to the injection strategy and the air intake conditions were optimized to enhance the engine performance (*i.e.*, Step 1 optimization). A total of seven operating parameters with crucial influences were chosen as the variables at three different loads in the previous study. Since the injection/wall interaction plays a critical role in the fuel/air mixture formation, the optimization of the injection parameters cooperated with the piston bowl geometry was further conducted at different load conditions in this study (*i.e.*, Step 2 optimization). The aim is to search for the most suitable piston bowl shape for the DMDF combustion mode over a wide load range. A total of 14 parameters were considered in the present work, including seven geometric parameters and seven engine operating parameters. The optimization specifications are listed in Table 5.

Table 5. Optimization specifications

| | Parameter | Range |
|---|---|---|
| Variables | Premix Ratio | (0.0, 1.0) |
| | SOI1 (°CA ATDC) | (-80.0, 10.0) |
| | SOI2 (°CA ATDC) | (SOI1, 10.0) |
| | MF1 | (0.0, 1.0) |
| | Spray angle (°) | (15, 85) |
| | Injection Pressure (MPa) | (50, 180) |
| | Compression Ratio | (12.0, 18.0) |
| | Normalized $Z_a$ | (0.0, 1.0) |
| | Normalized $Z_b$ | (0.0, 1.0) |
| | Normalized $X_b$ | (0.0, 1.0) |
| | Normalized $X_c$ | (0.0, 1.0) |
| | Normalized $R_a$ | (0.0, 1.0) |
| | Normalized $R_b$ | (0.0, 1.0) |
| | Normalized $R_c$ | (0.0, 1.0) |
| Constraints | EISFC (g/kWh) | <250.0 |
| | $T_{max}$ (K) | >1100.0 |
| | $NO_x$ (g/kWh) | <0.4 |
| | soot (g/kWh) | <0.01 |
| | PPRR (bar/°CA) | <15.0 |
| | $p_{max}$ (MPa) | <20.0 |
| | RI (MW/m$^2$) | <10.0 |

Table 6. Initial conditions at IVC timing at each load.

| | Low | Mid | High |
|---|---|---|---|
| $p_{ivc}$ (bar) | 1.51 | 1.99 | 3.30 |
| $T_{ivc}$ (K) | 392.2 | 306.1 | 315.5 |
| EGR (%) | 6.5 | 6.5 | 31.0 |

The seven geometric parameters are normalized $Z_a$, $Z_b$, $X_b$, $X_c$, $R_a$, $R_b$, and $R_c$, which determine the piston bowl shape, as illustrated in Figs. 1 and 2. The variation ranges of the geometric parameters are all from 0.0 to 1.0. The operating parameters relating to the direct fuel injection event include the two injection timings (*i.e.*, SOI1 and SOI2), injection pressure (*i.e.*, $p_{inj}$), mass fraction of the first injection (*i.e.*, MF1), and spray angle (SA). The variation ranges of the injection parameters can be found in Table 5. The SA is equal to a half of the injection plume included angle. Moreover, the premix ratio (*i.e.*, PR) of gasoline fuel and geometric compression ratio (*i.e.*, GCR) were also included in the variables to be optimized. In the engine simulations, the squish height was adjusted to match the desired GCR.

During the optimization process, the equivalent indicated specific fuel consumption (EISFC), $NO_x$, and soot emissions are selected as the objectives to urge the populations into the pleasant fuel economy and low-emission orientation. Meanwhile, several constraints are taken into consideration in order to guarantee the rationality of the optimal cases. In the optimization calculation, the peak in-cylinder temperature is kept above 1100 K to avoid misfire. For forbidding rough engine operations, the maximum in-cylinder pressure ($p_{max}$), ringing intensity (RI), and PPRR are limited under 19.0 MPa, 10 MW/$m^2$, and 15.0 bar/°CA, respectively [15]. The EISFC is restricted under 250 g/kWh to ensure satisfactory fuel economy, while the $NO_x$ and soot emission limits are set according to the Euro VI regulations (*i.e.*, 0.4 and 0.01 g/kWh, respectively). Moreover, the operating loads for optimization are located at 5.9, 11.9, and 22.6 bar, which are chosen from the baseline cases validated in Section 2.2. According to our previous study, the optimized air intake conditions including the initial temperature ($T_{ivc}$) and pressure ($p_{ivc}$) at IVC timing, as well as the EGR rate, are used in this work. Table 6 lists the setup of the initial conditions at the IVC timing for the optimization calculation at the three loads.

The optimization results of the present study are first compared with the previous optimization results to demonstrate the improvements gained from the piston bowl geometry optimization. Fig. 9 shows the evolution of the EISFC and $NO_x$ emissions for all the generated cases in the population at the various loads. The yellow and blue symbols represent the generated cases in the previous optimization (*i.e.*, Step 1 optimization) and the present optimization (*i.e.*, Step 2 optimization), respectively. Each case is colored by the generation number. A deeper color denotes a higher optimization degree. From the comparison of the Step 1 optimization to the Step 2 optimization, it can be found that EISFC is further decreased after the piston bowl geometry optimization while $NO_x$ emissions can still meet the Euro VI limit. The soot emissions of the optimal cases (*i.e.*, the deeper-color symbols) are also below the Euro VI limit, which is not illustrated in Fig. 9 due to space limitation. This well demonstrates the improvement of fuel economy without sacrificing the engine-out emissions in the Step 2 optimization. Overall, the above results indicate that the piston bowl geometry optimization further enhances the performance of the DMDF combustion mode at different loads.

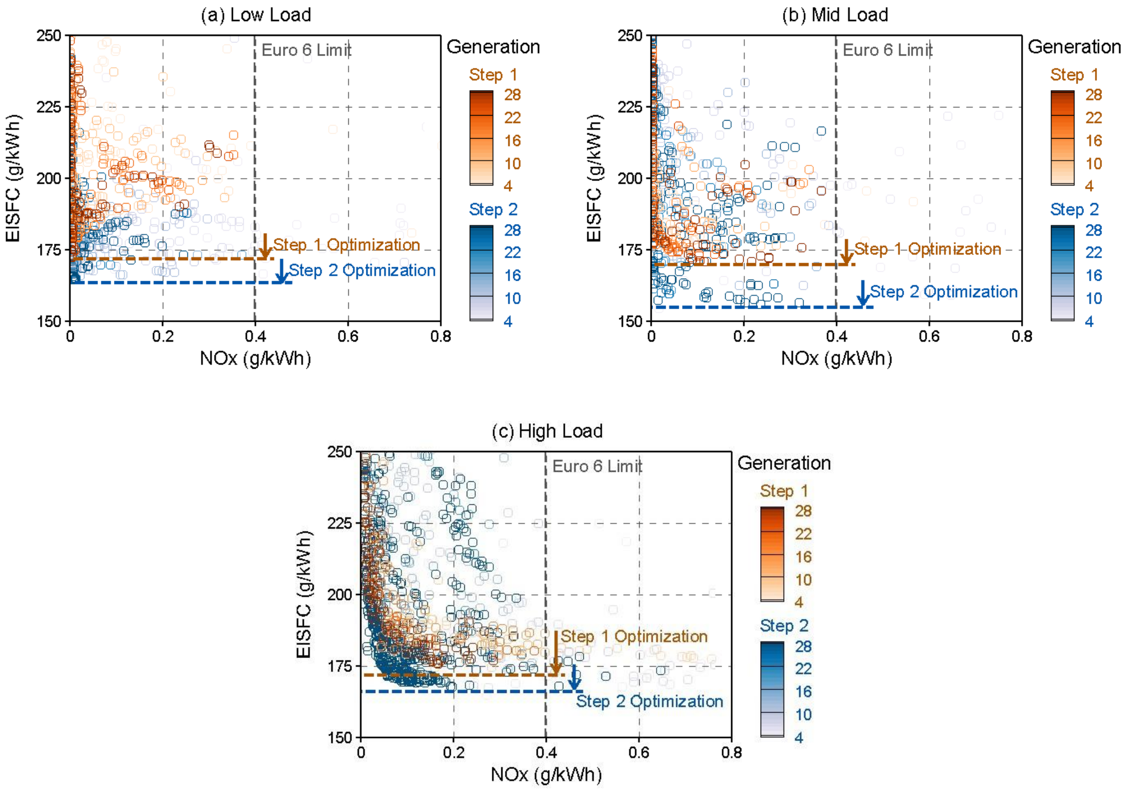


Fig. 9. Evolution of the EISFC and $NO_x$ emissions during the optimization at different loads.

Fig. 10 shows the comparison of the piston bowl shapes obtained during the optimization process at different loads. The dashed black line represents the baseline piston bowl shape for the DMDF mode [15]. The dashed grey line represents the top dead center position. The solid grey lines denote all the piston bowl profiles generated from the genetic algorithm. In this section, the cases with competitive fuel efficiency while meeting the Euro VI standards of the $NO_x$ and soot emissions are chosen as the optimal cases at each load. Furthermore, in order to provide more options for the DMDF piston bowl geometry design, among the optimal piston bowls, two typical shapes with distinguishing geometric characteristics are picked up to represent the optimal piston geometry at each load. The selected optimal cases are named as Low-A and Low-B for low load, Mid-A and Mid-B for mid load, and High-A and High-B for high load. As shown in Fig. 10, the optimal shapes are represented by the orange and blue lines.

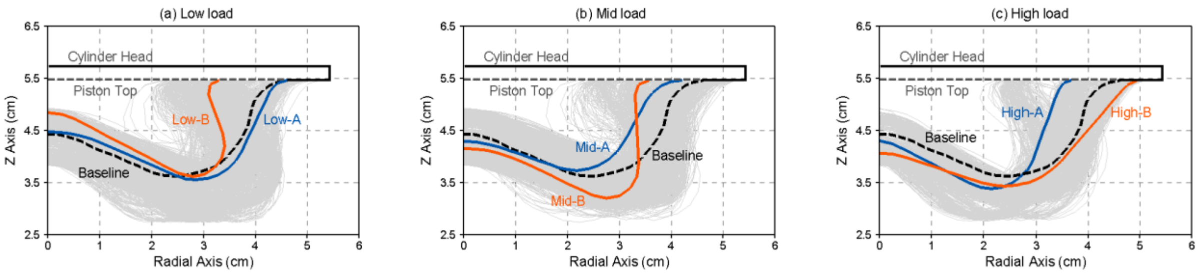


Fig. 10 Generated piston bowl shapes and typical optimal piston bowl shapes in the optimization at different loads.

It is seen from Fig. 10 that the optimal bowl geometries at low and mid loads contain both the open type and re-entrant type bowl, whereas the high load only contains the open type bowl. At low load, the optimal re-entrant type bowl (*i.e.*, case Low-B) features a smaller bowl width, while the optimal open type piston bowl (*i.e.*, case Low-A) features a similar bowl width compared with the baseline piston bowl, as shown in Fig. 10(a). At mid load, the optimal open type piston bowl (*i.e.*, case Mid-A) characterizes a relatively larger bowl width and smaller bowl depth, while the optimal re-entrant type bowl (*i.e.*, case Mid-B) characterizes a relatively smaller bowl width and larger bowl depth, as shown in Fig. 10(b). At high load, the two optimal cases feature a smaller bowl width (*i.e.*, case High-A) and a larger bowl width (*i.e.*, case High-B), respectively. Meanwhile, both of the two optimal cases at high load exhibit larger bowl depth compared with the baseline piston geometry, as shown in Fig. 10(c).

In order to demonstrate the engine improvements using the optimal piston bowl shapes, the optimal cases are compared to the previous optimal cases and the baseline cases in terms of fuel efficiency, $NO_x$ and soot emissions, as shown in Fig. 11. The grey bars and symbols represent the baseline cases and the optimal cases from the previous optimization (*i.e.*, Step 1 optimization). The orange and blue bars and symbols represent the optimal cases from the piston bowl geometry optimization (*i.e.*, Step 2 optimization). The left figures illustrate the comparisons of thermal efficiency, and the right figures provide the comparisons for $NO_x$ and soot emissions. As depicted in the left sub-figures of Fig. 11, significant improvement can be found for the thermal efficiency with the previous optimization (*i.e.*, Step 1) at the three loads. After optimizing the piston bowl shape combined with the injection parameters (*i.e.*, Step 2), the thermal efficiency is further improved. The thermal efficiency is increased up to 1.4%, 4.4%, and 1.4% for the low, mid, and high loads, respectively. It is worth noting that an indicated thermal efficiency up to 51.8% can be realized at mid load with the combined optimization. This well demonstrates the benefit gained for fuel economy from the piston bowl geometry optimization.

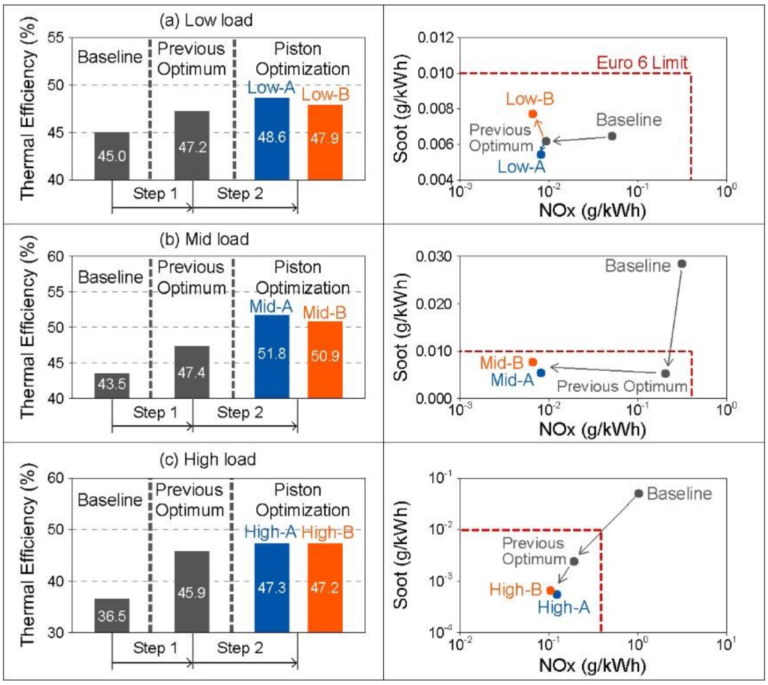


Fig. 11. Comparisons of thermal efficiency, $NO_x$ emissions, and soot emissions among the baseline cases and the optimal cases in Step 1 and Step 2 optimizations.

As for the right sub-figures of Fig. 11, both the $NO_x$ and soot emissions are continuously decreased after Step 1 and Step 2 optimizations at high load. At low and mid loads, the improvements of $NO_x$ and soot emissions for Step 2 optimization are not as significant as those for Step 1 optimization, but either $NO_x$ or soot emissions can still be further decreased to some extent after Step 2 optimization compared to the cases of Step 1 optimization. For both the optimal cases, the $NO_x$ and soot emissions can meet the Euro VI limits. Thus, it is concluded that the thermal efficiency can be significantly improved with the piston bowl geometry optimization without sacrificing $NO_x$ and soot emissions.

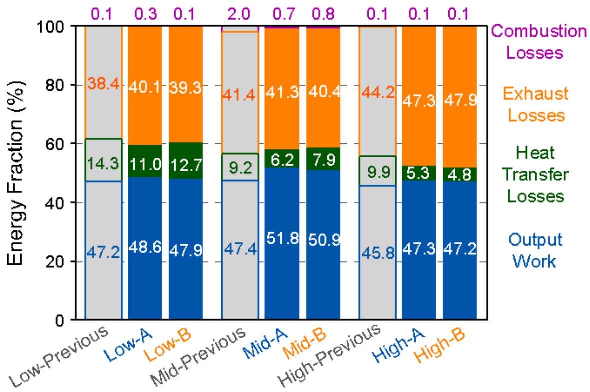


Fig. 12. Illustration of the energy fractions of optimal cases and baseline cases.

Furthermore, the energy analysis was conducted for investigating fuel efficiency benefits. As illustrated in Fig. 12, the energy fractions of the optimal cases in Step 2 optimization are compared with those of the previous optimal cases in Step 1 optimization. The bar colored by grey represents the previous optimal case while the other two represent the optimal cases from the piston bowl geometry optimization at each load. According to the first law of thermodynamics, the total input fuel energy is transferred into four parts during the combustion process, including output work, heat transfer losses, exhaust losses, and incomplete combustion (*i.e.*, combustion losses), as shown in Fig. 12. It is noted that the energy fraction of output work is directly related to the thermal efficiency depicted in Fig. 11. It can be seen from Fig. 12 that the purple bars are not obviously visible, which is due to the fact that the combustion losses are relatively low (less than 1%) under the whole load range. This is because that a majority of HC and CO emissions are reduced by the oxidation reactions in the late combustion stage. Thus, the engine-out emission levels of HC and CO are low. From the comparison of the optimal cases from the piston bowl geometry optimization with those from the previous optimization, it can be found that the improvement of the output work (*i.e.*, thermal efficiency) is mainly resulted from the decrease of the heat transfer losses at low and high loads. At mid load, the decreases of both the heat transfer losses and combustion losses contribute to the improvement of output work. This demonstrates the benefits of thermal efficiency gained from the piston bowl geometry optimization.

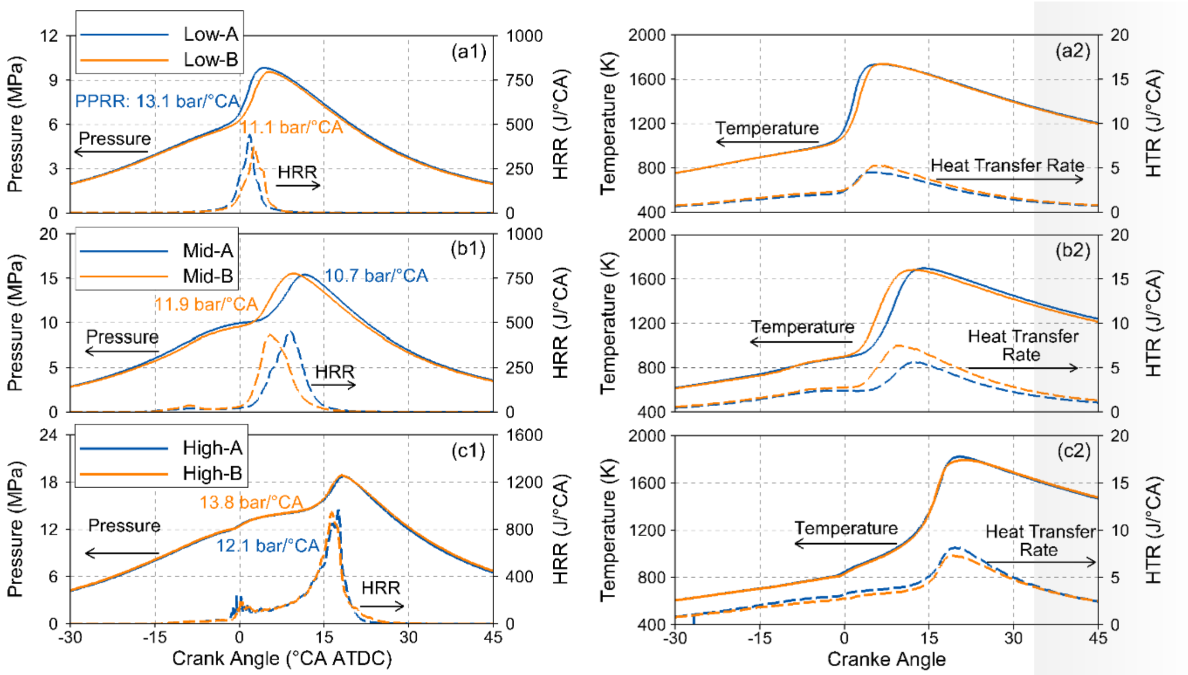


Fig. 13. Comparison of the in-cylinder pressure, HRR, temperature, and heat transfer rate (HTR) traces between the optimal cases.

Furthermore, the combustion process of the optimal cases is analyzed in detail for further explaining the improved performance after the piston bowl geometry optimization. Fig. 13 depicts the in-cylinder pressure, temperature, HRR, and heat transfer rate (HTR) traces of the optimal cases. Overall, from the comparisons of the pressure, temperature, and HRR, it is found that the traces at each load are very similar, especially for the high load condition, in spite of slight differences existing in the combustion phasing between the different optimal cases. This indicates that the different optimal cases exhibits similar combustion characteristics at each load. In terms of the comparison of the three loads, the combustion phasing is found to be retarded with increasing load, which is consistent with previous results [11, 19]. This is mainly aiming at controlling ringing intensity and preventing the engine knock. It can be seen from the denoted PPRR in Fig. 13 that at mid and high loads, by managing the combustion process and combustion phasing, the PPRR can meet the limit of 15 bar/°CA. At low load, although a relatively advanced combustion phasing is presented, the PPRR is still under the limit since the released fuel energy is much lower than those of mid and high loads.

Moreover, in order to understand the heat transfer process, the heat transfer rate (HTR) traces of the optimal cases at each load are also illustrated in Fig. 13. By comparing the HTR traces at each load, the differences in the heat transfer losses (see Fig. 12) can be explained. It can be found that the global HTR of cases Low-B, Mid-B, and High-A is higher than that of cases Low-A, Mid-A, and High-B, respectively. Thus, the heat transfer losses of cases Low-B, Mid-B, and High-A are relatively higher. However, the heat transfer process cannot be simply explained by the evolution of the global in-cylinder temperature since the piston bowl geometry and the combustion occurrence location also play critical roles. Thus, this will be explained in the following section.

## 3.2. Typical optimal piston bowl geometry and corresponding injection strategy

In this section, the optimal piston bowl shape coupled with the corresponding fuel injection strategy is summarized at each load. Table 7 lists the operating parameters of each optimal cases. Meanwhile, the fuel injection event and the fuel/air mixture formation process are analyzed as well. Fig. 14 shows the liquid fuel distribution after injection timing and the equivalence ratio distribution before ignition for cases Low-A and Low-B. As mentioned above, the optimal bowl shape for case Low-A is open type, while the optimal bowl shape for case Low-B is re-entrant type. Besides, as listed in Table 7, both of the two optimal cases utilize a similar compression ratio with that of the original engine setup (*i.e.*, 14.4) [15].

Table 7. Operating parameters of the optimal cases.

| | Low-A | Low-B | Mid-A | Mid-B | High-A | High-B |
|---|---|---|---|---|---|---|
| CR | 14.6 | 14.7 | 16.7 | 15.8 | 14.0 | 13.8 |
| PR | 97% | 97% | 90% | 76% | 96% | 96% |
| $p_{inj}$ (MPa) | 167 | 101 | 140 | 162 | 176 | 175 |
| SOI1 (°CA ATDC) | -57 | -51 | -56 | -79 | -28 | -26 |
| SOI2 (°CA ATDC) | - | - | -51 | -60 | -15 | -18 |

As for the fuel injection strategy, only the cases with the single injection strategy are retained in the genetic algorithm optimization at low load. By comparing Figs. 14(a1) and 14(b1), it is found that case Low-A is coupled with a relatively wider spray angle (SA) of 84.6°. In contrast with case Low-A, case Low-B is coupled with a relatively narrower SA of 76.2°, which is similar to that of the original experimental setup (*i.e.*, 75°) [15]. Figs. 14(a2) and 14(b2) illustrate the in-cylinder equivalence ratio distributions before ignition for cases Low-A and Low-B, respectively. From the comparison, it can be found that the high fuel concentration locations of the two cases are similar, which is owing to the combined effects of the piston bowl geometry and the fuel injection event. As can be seen, a stronger tumble flow is organized in the re-entrant piston bowl geometry in contrast to the open type bowl, which is also indicated by Miles and Andersson [44], as well as Lee et al. [45]. This results in larger flow velocity around the cylinder head and the piston wall near top dead center (TDC) for case Low-B. Thus, although a relatively lower injection pressure ($p_{inj}$) and a later SOI timing are employed for case Low-B, the injected fuel can also propagate to the similar location as that of case Low-A.

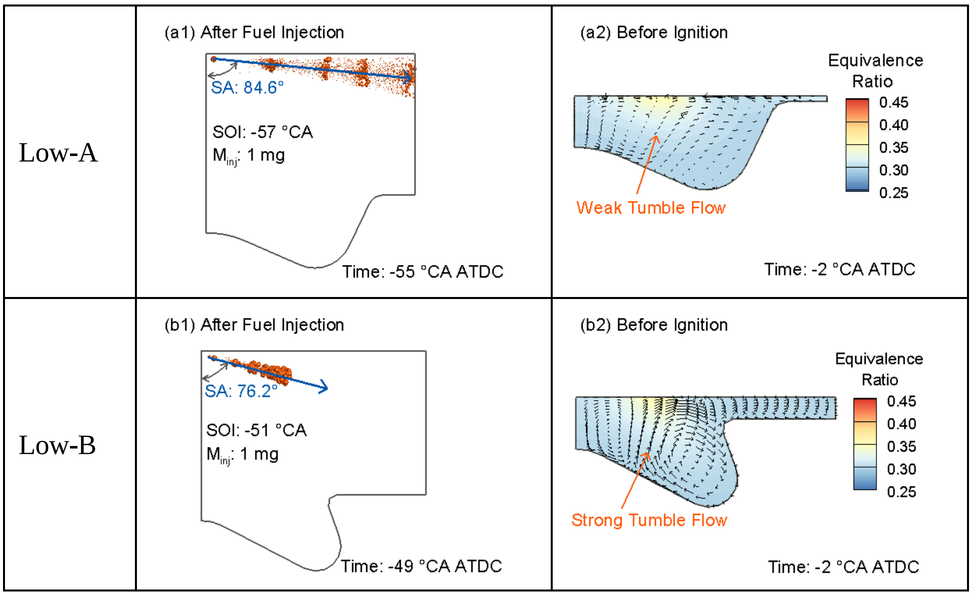


Fig. 14. Illustration of the optimal piston bowl shape, fuel injection and the fuel/air mixture formation at low load.

Fig. 15 depicts the liquid fuel distribution after injection timing and the equivalence ratio distribution before ignition for the optimal cases at mid load (*i.e.*, cases Mid-A and Mid-B). The shallow open piston bowl of case Mid-A is coupled with a relatively wider SA and lower injection pressure, as well as later fuel injection timings. On the contrary, the deep re-entrant piston bowl of case Mid-B is integrated with a relatively narrower SA and higher injection pressure, as well as earlier fuel injection timings. For case Mid-A, due to the lower $p_{inj}$ and wider SA compared to that of case Mid-B, the fuel spray penetration is relatively shorter, and the fuel mainly concentrates near the cylinder head, as shown in Fig. 15(a3), which is similar to the situation at low load. For case Mid-B, owing to the higher $p_{inj}$ and earlier fuel injection timings, the fuel penetration spray is much longer, which takes more fuel into the squish region. However, the strong squish flow in case Mid-B brings most of the injected fuel back into the bowl region, as shown in Fig. 15(b3). Meanwhile, the strong tumble flow resulted from the deep piston bowl geometry is helpful for the fuel/air mixing in case Mid-B with the employment of more injected fuel. Furthermore, as listed in Table 4, relatively higher CRs are employed in cases Mid-A and Mid-B for strengthening fuel efficiency. Thus, a significant improvement in thermal efficiency can be seen in Fig. 11. Meanwhile, with the help of lower initial temperature (see Table 3), the combustion phasing can be well controlled and the PPRR limit is maintained at mid load.

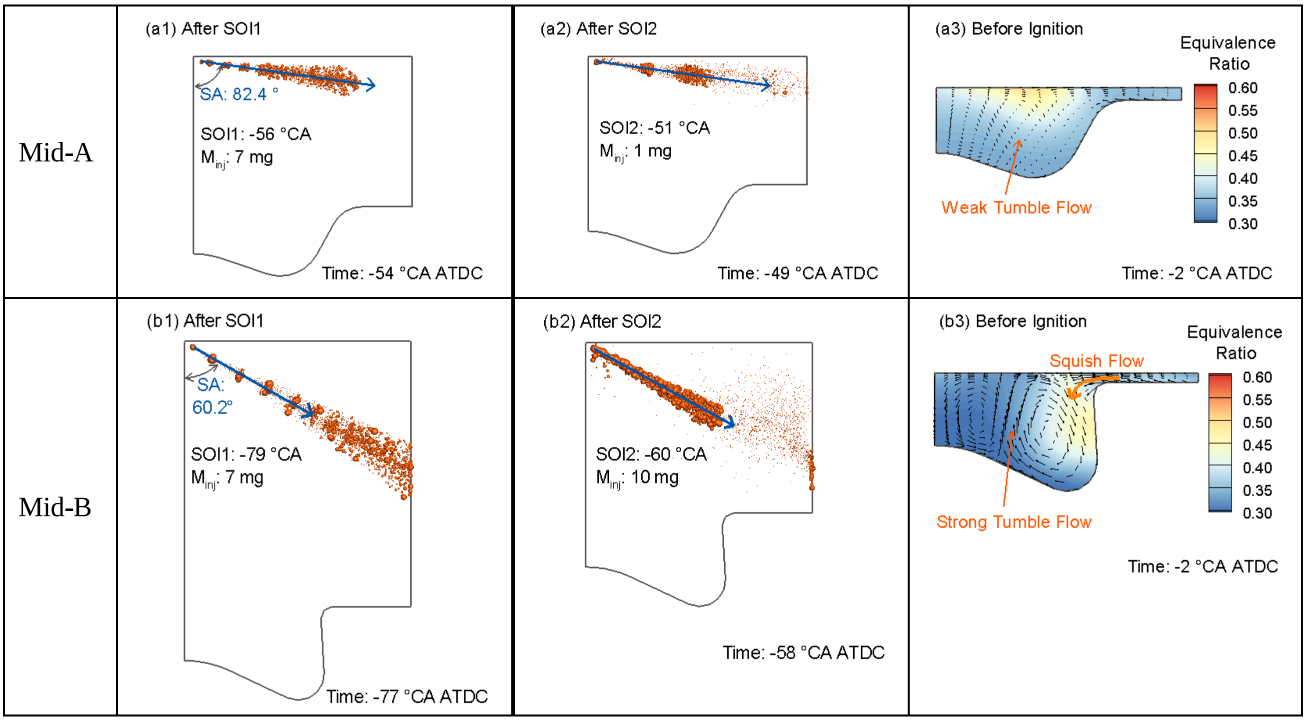

Fig. 15. Illustration of the optimal piston bowl shape, fuel injection and the fuel/air mixture formation at mid load.

As for high load, as shown in Fig. 16, both cases High-A and High-B employ the open type piston bowl. The difference is that case High-A utilizes a deep-narrow bowl geometry, while case High-B employs a shallow-wide open bowl geometry. Moreover, case High-A is coupled with a narrower SA, whereas case High-B uses a wider SA. In terms of fuel injection timings, both of the SOI1 and SOI2 timings of cases High-A and High-B are retarded compared with those of the optimal cases at low and mid loads. This is for avoiding advanced ignition, which can lead to high pressure rise rate and consequently engine knock at high load. Meanwhile, the relatively lower compression ratio employed by cases High-A and High-B (see Table 4) is also beneficial for controlling the PPRR. In such a way, a large fraction of gasoline can be premixed for the DMDF combustion mode at high load without exceeding the PPRR limit. Therefore, as shown in Table 4, the premix ratio of cases High-A and High-B can be increased to an equivalent level as that of mid and low loads. This is helpful for controlling the $NO_x$ and soot emissions owing to the premixed combustion enhancement.

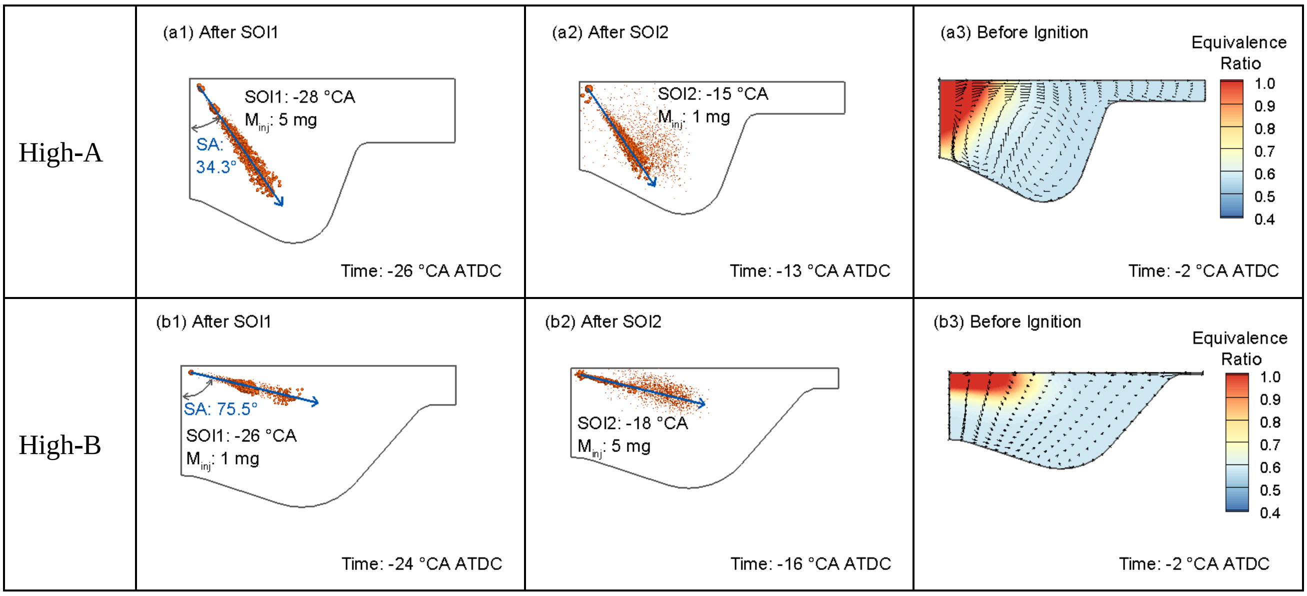


Fig. 16. Illustration of the optimal piston bowl shape, fuel injection and the fuel/air mixture formation at high load.

The late injection timings combined with the less injected fuel mass result in shorter fuel penetrations for cases High-A and High-B. Moreover, although the injection pressure is higher than lower loads (see Table 4), the increasing in-cylinder charge density resulted from the higher intake pressure at high load (see Table 3) restricts the propagation of the injected diesel fuel. Thus, the injected fuel mainly concentrates around the injection nozzle region, as shown in Figs. 16(a3) and 16(b3). Furthermore, from the comparison of the flow field of cases High-A and High-B, it is confirmed again that the deep and narrow bowl geometry can produce strong tumble flow compared with the shallow and wide piston geometry.

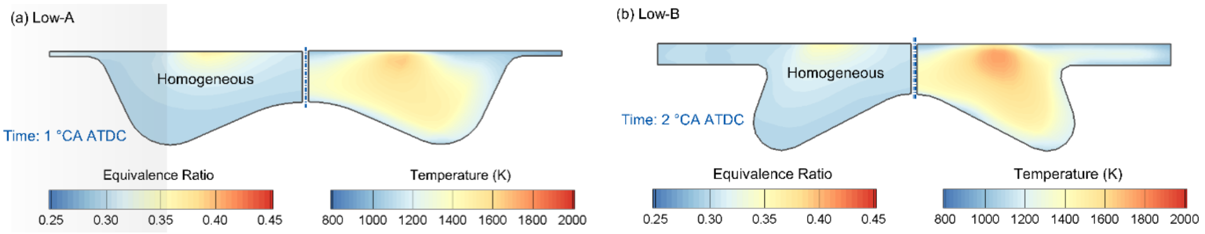


Fig. 17. In-cylinder equivalence ratio and temperature distributions at CA50 for cases Low-A and Low-B.

In order to further investigate the combustion characteristics of the optimal cases, the in-cylinder temperature and equivalence ratio distributions during the combustion process are further analyzed in this section. Figs. 17 to 19 depicts the in-cylinder temperature and equivalence ratio distributions at the time of 50% burning point (CA50) for the optimal cases of low, mid, and high loads, respectively. It can be found that the locations of the high fuel vapor concentration and the combustion occurrence are directly related to the fuel distribution pattern before ignition shown in the above figures, which is determined by the joint effects of piston bowl geometry and fuel injection strategy. As shown in Fig. 17, since the direct-injected fuel mass is lower, and a majority of fuel is premixed in the intake port, both cases Low-A and Low-B exhibit a homogeneous equivalence ratio distribution. This leads to the corresponding homogeneous combustion characteristics for both the optimal cases, which is helpful for the $NO_x$ and soot emission control. This is consistent with the previous results at low load operation [19].

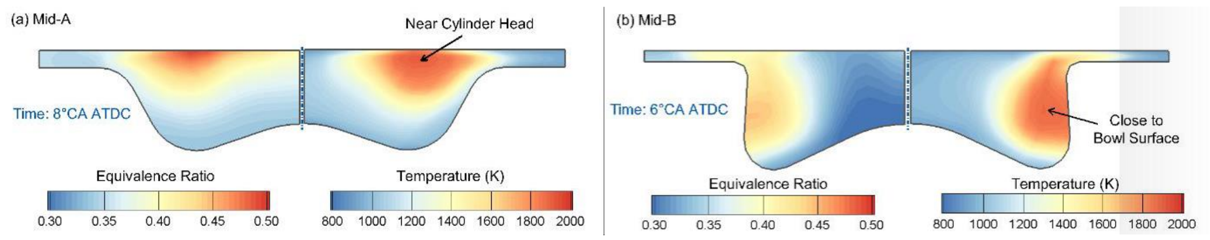


Fig. 18. In-cylinder equivalence ratio and temperature distributions at CA50 for cases Mid-A and Mid-B.

At mid load, with the increase of the injected fuel mass, the local equivalence ratio concentration is increased compared with the low load, as seen in Fig. 18. For case Mid-A, consistently with the low-load optimal cases, a high premix ratio (see Table 4) is utilized for enhancing the premix combustion, leading to pleasant $NO_x$ and soot emissions. For case Mid-B, although a higher direct-injected diesel fuel mass (*i.e.*, lower premix ratio) is employed, the local equivalence ratio concentration is lower than that of case Mid-A. This is because that the optimized deep re-entrant piston bowl geometry of case Mid-B produces a stronger tumble flow within the bowl region, leading to more sufficient premixing of the injected fuel with the in-cylinder charge before the combustion occurs. Thus, the Euro VI emission limits for the $NO_x$ and soot emissions can also be maintained for case Mid-B. Moreover, consistent with the vapor distribution of the direct-injected diesel fuel before ignition (see Fig. 15), the combustion occurrence location is near the cylinder head and close to the bowl surface for case Mid-A and case Mid-B, respectively.

At high load, although the injected mass is not further increased, the local equivalence ratio concentration is considerably elevated for the optimal cases, as illustrated in Fig. 19. This is mainly due to the shorter fuel spray penetration resulted from the later fuel injection timing and the increased in-cylinder charge density. Correspondingly, the combustion occurs near the cylinder axis region, which places the high-temperature region away from the piston bowl surface or the cylinder wall during the combustion phasing.

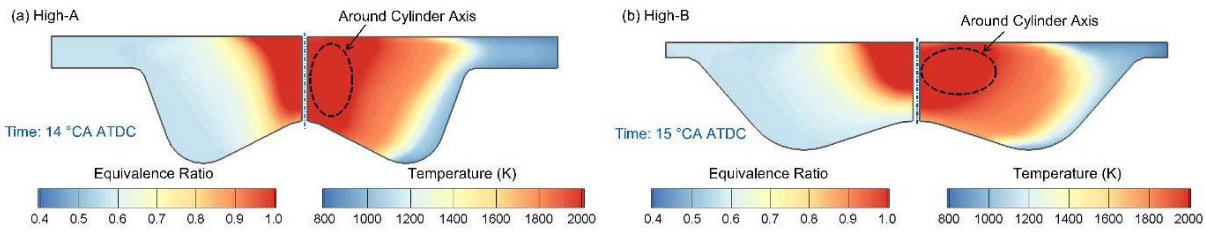


Fig. 19. In-cylinder equivalence ratio and temperature distributions at CA50 for cases High-A and High-B.

Moreover, the differences existing in the energy fraction of the heat transfer losses (see Fig. 12) between the optimal cases at each load can be further explained in this section. At low load, it is easy to find that the re-entrant type bowl of case Low-B exhibits a larger surface area compared with the open type bowl. Thus, although there is no obvious difference in the combustion temperature between cases Low-A and Low-B, the heat transfer energy fraction of case Low-B is higher than that of case Low-A due to the larger heat transfer area. Similarly, at mid load, the deep re-entrant piston bowl of case Mid-B yields a larger heat transfer surface. Meanwhile, for case Mid-B, the high-temperature region is closer to the bowl surface. Therefore, the heat transfer energy fraction is higher for case Mid-B than case Mid-A. At high load, as mentioned above, the high-temperature regions are away from the bowl surface for both the two optimal cases. This is beneficial for reducing heat transfer losses. Moreover, although the two optimal cases at high load employ the open type piston bowl, the heat transfer surface area of case High-B is smaller due to the opener and wider bowl geometry. Thus, the heat transfer energy fraction of case High-B is slightly higher than that of case High-A (see Fig. 12).

## 3.3. Correlation analysis

From the above discussion, it can be summarized that the in-cylinder fuel/air mixture formation and combustion processes are affected by the piston bowl geometry and the fuel injection strategy simultaneously. Thus, the performance of the DMDF combustion mode directly depends on the combined effects of the geometric parameters and the fuel injection parameters. For further understanding the influences of these parameters on the DMDF combustion mode, a correlation analysis was conducted to investigate the sensitivity of the engine performance to the various parameters at each load in this section. It is noted that 14 parameters were considered as the optimization variables in this study, which results in the significant complexity of the correlation analysis. Fortunately, a large number of cases (*i.e.*, citizens) were generated in the GA calculation process. In addition, with the introduction of the Sobol sequence sampling method for GA in this study, the distribution uniformity for the multi-dimensional variables of the numerous cases can be ensured, which provides a high-quality database for the correlation analysis in this section. The aim of the correlation analysis is to investigate the influence weight of each input parameter to the performance parameter including emissions for the DMDF concept.

Before the correlation analysis, the seven geometric parameters (see Fig. 3) were cut down and transferred into four key parameters for simplifying the analysis complexity. Fig. 20 depicts the definitions of the four new geometric parameters, including Depth1, Depth2, Width, and Open Extent (OE). The variable of Width is defined as the distance from the cylinder axis to the right edge of the piston bowl. Moreover, as indicated in Fig. 1, the piston bowl profile consists of two lines and three circle curves. The type of the piston bowl is directly determined by the orientation of Line2. Thus, in this section, a new parameter, *i.e.*, Open Extent, is introduced to describe the piston bowl type. The definition of Open Extent can be found in Fig. 20, which is equal to the ratio of R1 to R2 where R1 and R2 are the distances from the cylinder axis to the endpoints of Line2. Overall, the four new geometric parameters can well reflect the piston bowl characteristics.

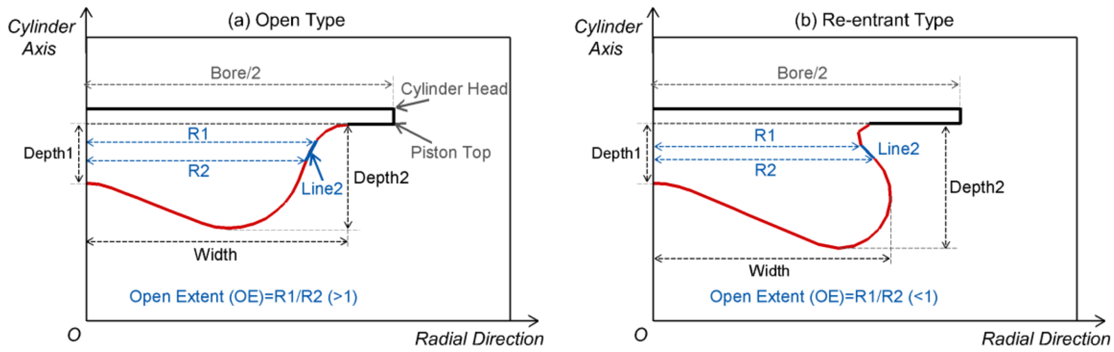


Fig. 20. Illustration of the key parameters for describing the bowl geometry of different types.

Subsequently, the correlation analysis was conducted between the input parameters and the performance parameters. The input parameters contain the four new geometric parameters and five injection parameters, including the SOI1, SOI2, MF1, SA, and $p_{inj}$. The performance parameters contain the energy fractions of heat transfer losses (HTL) and combustion losses (CL), as well as the $NO_x$ and soot emissions, which can reflect the combustion and emission characteristics of the DMDF engine. In this study, the correlation analysis is performed based on the Spearman Rank Correlation (SRC) coefficient [46]. This method is capable of providing the statistical relevance between the model input parameters and the target output parameters, and it has been widely used in engineering applications [47-49]. The SRC coefficient is defined as

$$\mathrm{SRC} = \frac{\mathrm{COV}(R_x, R_y)}{\sigma_{R_x}\sigma_{R_y}} \tag{1}$$

where $x$ and $y$ respectively represent the input and target output parameters, $R_x$ and $R_y$ respectively denote the rank values of parameters $x$ and $y$, $\mathrm{COV}(R_x, R_y)$ is the covariance of $R_x$ and $R_y$, and $\sigma_{Rx}$ and $\sigma_{Ry}$ represent the standard deviations of $R_x$ and $R_y$. In this study, the samples are chosen from the citizens generated in the GA calculation. After excluding the unreasonable cases with deteriorated combustion efficiency or rough engine operations, around 500 effective cases are retained as the samples for the correlation analysis at each load.

Figs. 21 to 23 illustrate the SRC coefficient of each input parameter to each performance parameter at low, mid, and high loads, respectively. In each figure, the left and right parts depict the SRC coefficient of the geometric parameters and the injection parameters, respectively. The range of the SRC coefficient is from −1.0 to 1.0. The impact of the input parameters on the performance parameters or the sensitivity of the performance parameters to the input parameters can be quantitatively described by the absolute value of the SRC coefficient. Furthermore, as shown in Figs. 21 to 23, the sum of the SRC coefficient can reflect the total contributions of the geometric or injection parameters to a single performance parameter.

As illustrated in Fig. 21, at low load, for $NO_x$ and soot emissions, the effects of the injection parameters are more significant compared to the geometric parameters. On the contrary, for heat transfer losses (HTL), the geometric parameters exert more obvious influences. As for the combustion losses (CL), the effects of the geometric parameters are equivalent to those of the injection parameters. At mid load, it is seen from Fig. 22 the sensitivity of the soot emissions and HTL to the input parameters increases, especially for the geometric parameters. For the $NO_x$ emissions and CL, the injection parameters still play more important roles in contrast to the geometric parameters. At high load, it is seen from Fig. 23 the sensitivity of the performance parameters to the injection parameters increase globally. The total SRC coefficients of the geometric parameters for the performance parameters are all lower than those of the injection parameters, except for HTL. This indicates that the fuel injection event becomes more crucial for managing the engine performance as load increases. Over the whole load range, among the injection parameters, the fuel injection timings and injection pressure contribute more significant influence to the performance parameters.

Overall, from the comparison results of Figs. 21 to 23, the sensitivity of the performance parameters at different loads can be summarized. For HTL, the geometric parameters contribute more significant effects than the injection parameters for all loads, although the sensitivity to the injection parameters is increased with at higher load. For CL, the effects of the geometric parameters are equivalent to those of the injection parameters at low load. With load increasing, the sensitivity of CL to the geometric parameters decreases, whereas the injection parameters still contribute obvious influences to the CL at mid and high loads. In terms of the emissions, the $NO_x$ emissions are more sensitive to the injection parameters than the geometric parameters over the whole load range. As for the soot emissions, the influences of both the injection and geometric parameters become more significant as load increases. Thus, it can be summarized that for HTL, CL, and soot emissions, the sensitivity to the injection parameters is lower at low load and is higher at mid and high loads. For the $NO_x$ emissions, the sensitivity to the injection parameters is lower at low and mid loads. By contrast, at high load, the sensitivity of the $NO_x$ emissions to the injection parameters is relatively higher. Overall, it can be concluded that the fuel injection event becomes more important for managing the engine performance and emissions as load increases

Moreover, the key individual input parameters with crucial influences on the performance parameter can be further summarized as well. Among the geometric parameters, the most influential parameters are Width and Open Extent (OE), which is also indicated in Ref. [44]. In particular, the two parameters exert obvious and consistent impacts on heat transfer losses over the whole load range. It is indicated from Figs. 21 to 23 that the heat transfer losses can be reduced with a wider and more open piston bowl. As for the injection parameters, the fuel injection timings (*i.e.*, SOI1 and SOI2) and injection pressure (*i.e.*, $p_{inj}$) contribute more influences on the engine performance in contrast to other parameters when load increases.

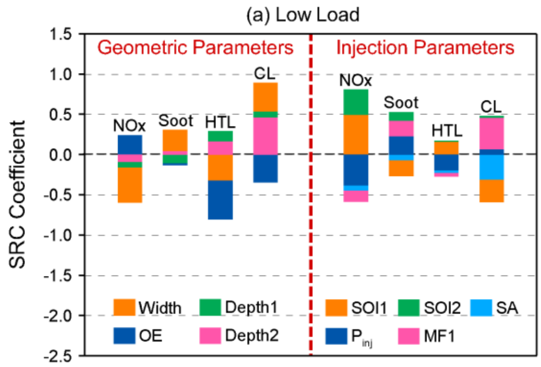


Fig. 21. SRC coefficient of each input parameter for each performance parameter at low load.

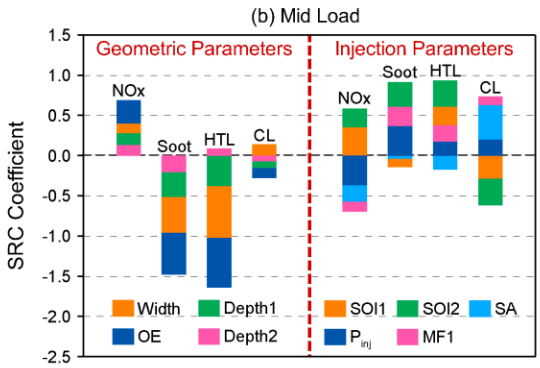


Fig. 22. SRC coefficient of each input parameter for each performance parameter at mid load.

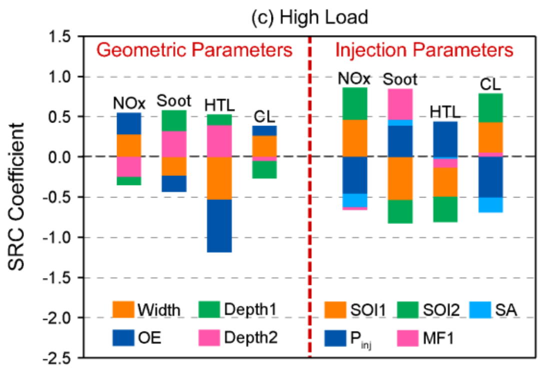


Fig. 23. SRC coefficient of each input parameter for each performance parameter at high load.

# 4. Conclusions

Based on the DMDF combustion mode, the combined optimization of the piston bowl geometry and the fuel injection strategy was performed over a wide load range using an improved genetic algorithm coupled with the CFD simulation in this work. The optimal piston bowl shape coupled with the desired injection strategy at different loads was summarized, and the improvements of engine performance were analyzed compared with the previous results about the DMDF studies. Furthermore, a correlation analysis was conducted to investigate the sensitivity of engine performance to the geometric parameters and the injection parameters. The major conclusions can be summarized as follows.

1. By optimizing the piston bowl geometry coupled with the injection strategy, the behavior of the DMDF combustion mode is further enhanced at various loads. Over the test load range, the thermal efficiency is increased up to 1.4%, 4.4%, and 1.4% for the low, mid, and high loads, respectively. An indicated thermal efficiency up to 51.8% can be realized at mid load with the combined optimization. Meanwhile, for all the optimal cases, the $NO_x$ and soot emissions can meet the Euro VI limits.
2. The optimal piston bowl shape integrated with the corresponding injection strategy is summarized at each load, providing guidelines for the piston structure design. At low load, both of the re-entrant and open type piston bowl can be equipped. At mid load, the shallow open piston bowl and the deep re-entrant piston bowl can be utilized. At high load, the open type piston bowl is preferred. The combustion occurrence location is determined by the combined effect of the piston bowl geometry and the injection strategy. Overall, the re-entrant type or deep piston bowls are good at organizing strong in-cylinder flow, which is beneficial for the fuel/air mixing.
3. The fuel injection event becomes more important for managing the engine performance and emissions as load increases. Among the injection parameters, fuel injection timings (*i.e.*, SOI1 and SOI2) and injection pressure (*i.e.*, $p_{inj}$) contribute more influences on the engine performance and emissions.
4. The piston bowl geometric parameters contribute more significant effects on the heat transfer losses than the injection parameters for all loads, although the sensitivity to the injection parameters is increased with the higher

load. Among the geometric parameters, the most influential parameters are Width and Open Extent (OE). The heat transfer losses can be reduced with a wider and more open piston bowl.

The future research work will be focused on applying the numerical optimization results in practical engine experiments. The optimized piston bowl shapes at different loads are will also be integrated into one general shape for simultaneously considering engine performance and emissions at various operating conditions.

# Acknowledgments

This work was partially supported by the National Natural Science Foundation of China (Grant Nos. 51961135105 and 91641117) and Postdoctoral Research Foundation of China (Grant Nos. 2019M661094 and 2020T130075). The experimental results used in this investigation were obtained in a project funded by VOLVO Group Trucks Technology. The authors also acknowledge FEDER and Spanish Ministerio de Economía y Competitividad for partially supporting this research through TRANCO project (TRA2017-87694-R) and the Universitat Politècnica de València for partially supporting this research through Convocatoria de ayudas a Primeros Proyectos de Investigación (PAID-06-18).

# References


[1] Johnson TV. Diesel emission control in review. SAE Technical Paper; 2009; no. 2009-01-0121.

[2] Musculus MP, Miles PC, Pickett LM. Conceptual models for partially premixed low-temperature diesel combustion. Prog Energy Combust Sci. 2013;39(2):246-83.

[3] Reitz RD, Duraisamy G. Review of high efficiency and clean reactivity controlled compression ignition (RCCI) combustion in internal combustion engines. Prog Energy Combust Sci. 2015;46:12-71.

[4] Benajes J, García A, Pastor JM, Monsalve-Serrano J. Effects of piston bowl geometry on reactivity controlled compression ignition heat transfer and combustion losses at different engine loads. Energy. 2016;98:64-77.

[5] Li Y, Jia M, Chang Y, Kokjohn SL, Reitz RD. Thermodynamic energy and exergy analysis of three different engine combustion regimes. Appl Energy. 2016;180:849-58.

[6] Gong C, Li Z, Yi L, Liu F. Comparative study on combustion and emissions between methanol port-injection engine and methanol direct-injection engine with $H_2$-enriched port-injection under lean-burn conditions. Energy Convers Manage. 2019;200:112096.

[7] Tong L, Wang H, Zheng Z, Reitz R, Yao M. Experimental study of RCCI combustion and load extension in a compression ignition engine fueled with gasoline and pode. Fuel. 2016;181:878-86.

[8] Lim JH, Reitz RD. High load (21 bar IMEP) dual fuel RCCI combustion using dual direct injection. J Eng Gas Turbines Power. 2014;136(10):101514(1-10).

[9] Wang Y, Yao M, Li T, Zhang W, Zheng Z. A parametric study for enabling reactivity controlled compression ignition (RCCI) operation in diesel engines at various engine loads. Appl Energy. 2016;175:389-402.

[10] Molina S, García A, Pastor JM, Belarte E, Balloul I. Operating range extension of RCCI combustion concept from low to full load in a heavy-duty engine. Appl Energy. 2015;143:211-27.

[11] Xu G, Jia M, Li Y, Chang Y, Wang T. Potential of reactivity controlled compression ignition (RCCI) combustion coupled with variable valve timing (VVT) strategy for meeting Euro 6 emission regulations and high fuel efficiency in a heavy-duty diesel engine. Energy Convers Manage. 2018;171:683-98.

[12] Xu GF, Jia M, Li YP, Chang YC, Liu H, Wang TY. Evaluation of variable compression ratio (VCR) and variable valve timing (VVT) strategies in a heavy-duty diesel engine with reactivity controlled compression ignition (RCCI) combustion under a wide load range. Fuel. 2019;253:114-28.

[13] Mikulski M, Balakrishnan PR, Doosje E, Bekdemir C. Variable valve actuation strategies for better efficiency load range and thermal management in an RCCI engine. SAE Technical Paper; 2018; no. 2018-01-0254.

[14] Benajes J, Pastor JV, García A, Boronat V. A RCCI operational limits assessment in a medium duty compression ignition engine using an adapted compression ratio. Energy Convers Manage. 2016;126:497-508.

[15] Benajes J, García A, Monsalve-Serrano J, Boronat V. Achieving clean and efficient engine operation up to full load by combining optimized RCCI and dual-fuel diesel-gasoline combustion strategies. Energy Convers Manage. 2017;136:142-51.

[16] Benajes J, García A, Monsalve-Serrano J, Lago Sari R. Fuel consumption and engine-out emissions estimations of a light-duty engine running in dual-mode RCCI/CDC with different fuels and driving cycles. Energy. 2018;157:19-30.

[17] García A, Monsalve-Serrano J, Villalta D, Sari R. Fuel sensitivity effects on dual-mode dual-fuel combustion operation for different octane numbers. Energy Convers Manage. 2019;201:112137.

[18] Macián V, Bermúdez V, Villalta D, Soto L. Effects of low-pressure EGR on gaseous emissions and particle size distribution from a dual-mode dual-fuel (DMDF) concept in a medium-duty engine. Appl Therm Eng.

2019;163:114245.

[19] Xu G, Monsalve-Serrano J, Jia M, García A. Computational optimization of the dual-mode dual-fuel concept through genetic algorithm at different engine loads. Energy Convers Manage. 2020;208:112577.

[20] García A, Gil A, Monsalve-Serrano J, Lago Sari R. OMEx-diesel blends as high reactivity fuel for ultra-low NOx and soot emissions in the dual-mode dual-fuel combustion strategy. Fuel. 2020;275:117898.

[21] García A, Monsalve-Serrano J, José Sanchís E, Fogué-Robles Á. Exploration of suitable injector configuration for dual-mode dual-fuel engine with diesel and OMEx as high reactivity fuels. Fuel. 2020;280:118670.

[22] Dempsey AB, Walker NR, Reitz RD. Effect of piston bowl geometry on dual fuel reactivity controlled compression ignition (RCCI) in a light-duty engine operated with gasoline/diesel and methanol/diesel. SAE Technical Paper; 2013; no. 2013-01-0264.

[23] Park SW. Optimization of combustion chamber geometry for stoichiometric diesel combustion using a micro genetic algorithm. Fuel Process Technol. 2010;91(11):1742-52.

[24] Xu L, Bai X-S, Li Y, Treacy M, Li C, Tunestål P, Tunér M, Lu X. Effect of piston bowl geometry and compression ratio on in-cylinder combustion and engine performance in a gasoline direct-injection compression ignition engine under different injection conditions. Appl Energy. 2020;280:115920.

[25] Nazemian M, Neshat E, Saray RK. Effects of piston geometry and injection strategy on the capacity improvement of waste heat recovery from RCCI engines utilizing DOE method. Appl Therm Eng. 2019;152:52-66.

[26] Lee S, Park S. Optimization of the piston bowl geometry and the operating conditions of a gasoline-diesel dual-fuel engine based on a compression ignition engine. Energy. 2017;121:433-48.

[27] Badra J, khaled F, Sim J, Pei Y, Viollet Y, Pal P, Futterer C, Brenner M, Som S, Farooq A, Chang J.

Combustion system optimization of a light-duty GCI engine using cfd and machine learning. SAE Technical Paper; 2020; no. 2020-01-1313.

[28] Amsden AA. KIVA-3V: A block structured KIVA program for engines with vertical and canted valves. USA: Los Alamos National Laboratory Technical Report; 1997. LA-13313-MS.

[29] Wang BL, Lee CW, Reitz RD, Miles PC, Han Z. A generalized renormalization group turbulence model and its application to a light-duty diesel engine operating in a low-temperature combustion regime. Int J Engine Res. 2012;14(3):279-92.

[30] Zhang Y, Jia M, Liu H, Xie M, Wang T, Zhou L. Development of a new spray/wall interaction model for diesel spray under PCCI-engine relevant conditions. Atomization and Sprays. 2014;24(1):41-80.

[31] Zhang Y, Jia M, Liu H, Xie M. Development of an improved liquid film model for spray/wall interaction under engine-relevant conditions. Int J Multiphase Flow. 2016;79:74-87.

[32] Yi P, Long W, Jia M, Tian J, Li B. Development of a quasi-dimensional vaporization model for multi-component fuels focusing on forced convection and high temperature conditions. Int J Heat Mass Transfer. 2016;97:130-45.

[33] Zhang Y, Jia M, Yi P, Liu H, Xie M. An efficient liquid film vaporization model for multi-component fuels considering thermal and mass diffusions. Appl Therm Eng. 2017;112:534-48.

[34] Cao J, Jia M, Niu B, Chang Y, Xu Z, Liu H. Establishment of an improved heat transfer model based on an enhanced thermal wall function for internal combustion engines operated under different combustion modes. Energy Convers Manage. 2019;195:748-59.

[35] Nordin PAN. Complex chemistry modeling of diesel spray combustion. Sweden: Chalmers University of Technology; 2001. PhD Thesis.

[36] Ricart LM, Reltz RD, Dec JE. Comparisons of diesel spray liquid penetration and vapor fuel distributions

with in-cylinder optical measurements. J Eng Gas Turbines Power. 2000;122(4):588-95.

[37] Kee RJ, Rupley FM, Meeks E, Miller JA. Chemkin-III: A fortran chemical kinetics package for the analysis of gas phase chemical and plasma kinetics. USA: Sandia National Laboratory Technical Report; 1996. SAND96-8216.

[38] Chang Y, Jia M, Li Y, Xie M. Application of the optimized decoupling methodology for the construction of a skeletal primary reference fuel mechanism focusing on engine-relevant conditions. Front Mech Eng. 2015;1:1-11.

[39] Xu G, Jia M, Li Y, Chang Y, Liu H, Wang T. Evaluation of variable compression ratio (VCR) and variable valve timing (VVT) strategies in a heavy-duty diesel engine with reactivity controlled compression ignition (RCCI) combustion under a wide load range. Fuel. 2019;253:114-28.

[40] Li Y, Jia M, Chang Y, Xu Z, Xu G, Liu H, Wang T. Principle of determining the optimal operating parameters based on fuel properties and initial conditions for RCCI engines. Fuel. 2018;216:284-95.

[41] Kim M, Reitz RD, Kong SC. Modeling early injection processes in hsdi diesel engines. SAE Technical Paper; 2006; no. 2006-01-0056.

[42] Deb K, Pratap A, Agarwal S, Meyarivan T. A fast and elitist multiobjective genetic algorithm: NSGA-II. IEEE Trans Evol Comput. 2002;6(2):182-97.

[43] Navid A, Khalilarya S, Abbasi M. Diesel engine optimization with multi-objective performance characteristics by non-evolutionary Nelder-Mead algorithm: Sobol sequence and latin hypercube sampling methods comparison in doe process. Fuel. 2018;228:349-67.

[44] Miles PC, Andersson Ö. A review of design considerations for light-duty diesel combustion systems. Int J Engine Res. 2015;17(1):6-15.

[45] Lee J, Lee S, Kim J, Kim D. Bowl shape design optimization for engine-out PM reduction in heavy duty

diesel engine. SAE Technical Paper; 2015; no. 2015-01-0789.

[46] Chang Y, Jia M, Niu B, Xie M, Zhou C. Reduction of detailed chemical mechanisms using reaction class-based global sensitivity and path sensitivity analyses. Energy Fuels. 2019;33(9):9289-301.

[47] Fridlyand A, Johnson MS, Goldsborough SS, West RH, McNenly MJ, Mehl M, Pitz WJ. The role of correlations in uncertainty quantification of transportation relevant fuel models. Combust Flame. 2017;180:239-49.

[48] Chang Y, Jia M, Niu B, Zhang Y, Xie M, Li Y. Construction and assessment of reduced oxidation mechanisms using global sensitivity analysis and uncertainty analysis. Proc Combust Inst. 2019;37(1):751-61.

[49] Hébrard É, Tomlin AS, Bounaceur R, Battin-Leclerc F. Determining predictive uncertainties and global sensitivities for large parameter systems: A case study for n-butane oxidation. Proc Combust Inst. 2015;35(1):607-16.

# Computational optimization of the piston bowl geometry for the different combustion regimes of the dual-mode dual-fuel (DMDF) concept through an improved genetic algorithm

Guangfu Xu [a], Antonio García [b], Ming Jia [a, *], Javier Monsalve-Serrano [b]

[a] Key Laboratory of Ocean Energy Utilization and Energy Conservation of Ministry of Education, Dalian University of Technology, Dalian, 116024, P.R. China

[b] CMT - Motores Térmicos, Universitat Politècnica de València, Camino de Vera s/n, 46022 Valencia, Spain

* Corresponding author:

Ming Jia

School of Energy and Power Engineering

Dalian University of Technology

Dalian, 116024

P.R. China

**Tel:** +86-411-84706722

**Fax:** +86-411-84706722

**Email:** jiaming@dlut.edu.cn

# Computational optimization of the piston bowl geometry for the different combustion regimes of the dual-mode dual-fuel (DMDF) concept through an improved genetic algorithm

Guangfu Xu [a], Antonio García [b], Ming Jia [a, *], Javier Monsalve-Serrano [b]

[a] Key Laboratory of Ocean Energy Utilization and Energy Conservation of Ministry of Education, Dalian University of Technology, Dalian, 116024, P.R. China

[b] CMT - Motores Térmicos, Universitat Politècnica de València, Camino de Vera s/n, 46022 Valencia, Spain

## Abstract

Focusing on the dual-mode dual-fuel (DMDF) combustion concept, a combined optimization of the piston bowl geometry with the fuel injection strategy was conducted at various loads. An improved genetic algorithm was introduced in this study, which is superior in searching for the global optimal solutions. The optimal piston bowl shape coupled with the corresponding injection strategy was summarized at the various loads. The results show that the piston bowl geometry optimization can further improve the thermal efficiency with 1.4%, 4.4%, and 1.4% percentage points for the low, mid, and high loads, respectively. An indicated thermal efficiency up to 51.8% can be realized at mid load. Meanwhile, for all the optimal cases, $NO_x$ and soot emissions can meet the Euro VI limits.

At low and mid loads, both the open and re-entrant type piston bowl can be equipped, while the high load only prefers the open type piston bowl for the DMDF mode. The re-entrant type or deep piston bowls are superior in organizing strong in-cylinder flow, which is beneficial for the fuel/air mixing. The open type or shallow piston bowls are helpful for reducing the heat transfer losses owing to the less heat transfer surface area. Furthermore, a correlation analysis was conducted to investigate the sensitivity of engine performance to the piston geometric parameters and

injection parameters. It is concluded that the fuel injection event becomes more important for managing the engine performance as load increases. Among the injection parameters, the influence of the fuel injection timings and injection pressure on engine performance is more obvious. The piston geometric parameters play more significant roles in the heat transfer losses than the injection parameters for all loads. Among the geometric parameters, the most influential parameters are the width and open extent of the piston bowl. The heat transfer loss energy fraction can be well decreased with a wider and more open piston bowl.

**Keywords**: Piston bowl geometry optimization; Dual-mode dual-fuel (DMDF); Genetic algorithm; Fuel efficiency; Correlation analysis

# Graphical abstract

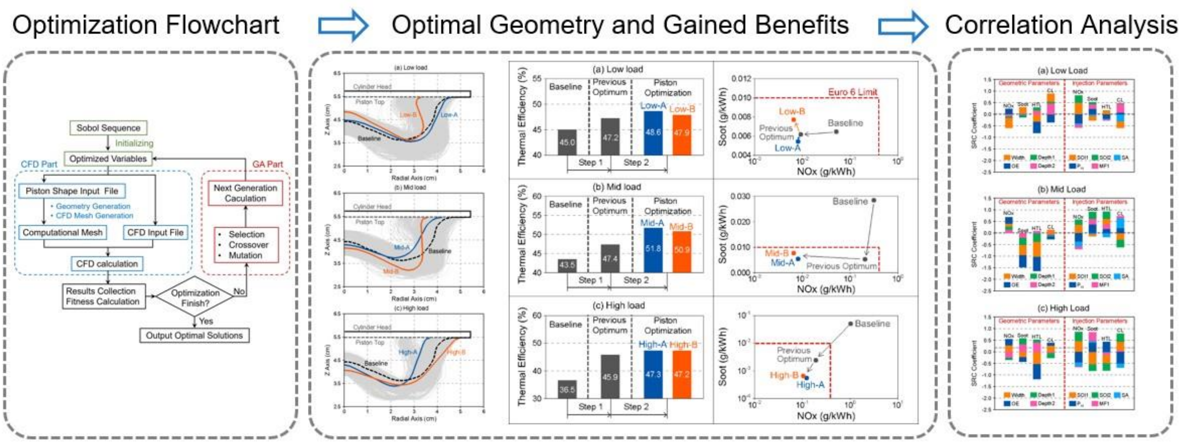

**Nomenclature**

| | |
|---|---|
| 1D | one-dimensional |
| 3D | three-dimension |
| ATDC | after top dead center |
| CA50 | 50% burn point |
| CDC | conventional diesel combustion |
| CFD | computational fluid dynamics |
| CL | combustion losses |
| CO | carbon monoxide |
| DI | direct injection |
| DMDF | dual-mode dual-fuel |
| DOE | design of experiment |
| DPF | diesel particulate filter |
| EGR | exhaust gas recirculation |
| EISFC | equivalent indicated specific fuel consumption |
| EPA | Environmental Protection Agency |
| GA | genetic algorithm |
| GCR | geometric compression ratio |
| HRR | heat release rate |
| HC | hydrocarbon |
| HCCI | homogeneous charge compression ignition |
| HTL | heat transfer losses |
| HTR | heat transfer rate |
| ICE | internal combustion engine |
| IMEP | indicated mean effective pressure |
| ISFC | indicated specific fuel consumption |
| IVC | intake valve closing |
| LHV | lower heating value |
| LTC | low-temperature combustion |
| MF1 | mass fraction of the first injection |
| NSGA | non-dominated sorting genetic algorithm |
| $NO_x$ | nitrogen oxides |
| OE | Open Extent |
| $p_{inj}$ | injection pressure |
| $p_{ivc}$ | inital pressure at IVC timing |
| $p_{max}$ | maximum in-cylinder pressure |
| PPC | partially premixed combustion |
| PPRR | peak pressure rise rate |
| PR | premix ratio |
| RCCI | reactivity controlled compression ignition |
| RI | ringing intensity |
| SA | spray angle |
| SCR | selective catalytic reduction |
| SOI | start of injection |
| SOI1 | start of injection timing for first pulse |
| SOI2 | start of injection timing for second pulse |
| SRC | Spearman Rank Correlation |
| TDC | top dead center |
| $T_{ivc}$ | initial temperature at IVC timing |
| VVT | variable valve timing |

# 1. Introduction

The increasingly stringent emission regulations and urgent energy shortage are bringing huge challenges for the internal combustion engine (ICE) research community. Improving fuel economy and eliminating engine-out emissions are still the major objectives and main investigation fields for ICE researchers. Currently, the selective catalyst reduction (SCR) and diesel particulate filter (DPF) systems have been widely adopted by engine manufacturers as the aftertreatment devices for decreasing nitrogen oxides ($NO_x$) and soot emissions, respectively. Although their effectiveness has been demonstrated, the engine layout complexity and cost are increased as well [1]. Alternatively, the low-temperature combustion (LTC) strategy [2] was proposed, which yields great potential of reducing $NO_x$ and soot emissions while maintaining pleasant fuel economy owing to the characteristics of homogeneous-mixing and low-temperature combustion process.

Among the LTC modes, reactivity controlled compression ignition (RCCI) [3] concept attracts more scientific interest due to the flexible control over the combustion process with the dual-fuel system. In RCCI mode, the fuel concentration and reactivity stratification can be accomplished relying on delivering the low-reactivity fuel by port fuel injection (PFI) and the high-reactivity fuel by in-cylinder direct injection (DI), respectively. By adjusting the low-reactivity fuel percentage and the direct injection event, the fuel distribution and reactivity can be tuned, and a flexible operation in a wide operating range can be realized [4]. In spite of this, the RCCI strategy is still facing the problems of low combustion efficiency at low load [5, 6] and serious engine noise at high load [7]. Thus, the improvement of the RCCI strategy over a wide operating range is still needed.

Up to now, many investigations focus on the extension of the RCCI operation range. Lim et al. [8] found that extremely low $NO_x$ and soot emissions, as well as the indicated thermal efficiency of 48.7% can be reached for a gasoline/diesel RCCI engine at high load up to 21 bar of the indicated mean effective pressure (IMEP). Wang et al. [9] demonstrated the effectiveness of exhaust gas recirculation (EGR) rate for preventing excessively high peak pressure rise rate (PPRR) and extending the RCCI mode to higher loads. Meanwhile, it was found that the employment of gasoline/diesel dual-fuel RCCI mode at mid and high loads can maintain ultra-low $NO_x$ and soot emissions, while the diesel LTC strategy with single fuel injection is more attractive for low load conditions.

Molina et al. [10] extended the RCCI operating range by employing a multiple direct-injection strategy combined with the Miller cycle. At low load, the double injection strategy was used for managing the combustion phasing and emissions. At high load, the injection shifts into a single injection for triggering the ignition and maintaining mild combustion. Xu et al. [11, 12] optimized the key parameters of an RCCI engine couple with the the variable valve timing (VVT) and variable compression ratio (VCR) strategies at various load conditions. The results indicated that the Euro VI limit can be well maintained over the whole load range, whereas the trade-off of the $NO_x$ and soot emissions at high load is difficult to solve. Mikulski et al. [13] found that early intake valve closing is beneficial for the RCCI operation at high load, whereas retarding the intake valve opening timing can reduce combustion losses.

Benajes et al. [14] indicated that 80% of the nominal operating range for conventional diesel engines can be covered by the RCCI operation by employing appropriate fuel ratio, EGR rate, and intake temperature, while the PPRR limit will not be surpassed. Based on that study, a dual-mode dual-fuel (DMDF) concept was proposed by Benajes et al. [15]. In the DMDF concept, the combustion mode was shifted regarding the engine load. At low load, the highly-premixed RCCI operation was employed for enhancing the engine efficiency and obtaining low levels of emissions. At high load, the combustion mode was switched to diffusive combustion for slowing down the combustion rate and meeting the engine mechanical restriction. Recently, a series of efforts were made for the development of the DMDF concept, as summarized in Table 1.

Table. 1. A Summary of the main papers published on DMDF combustion mode

| Reference | Contents of the research | Main Conclusions |
|---|---|---|
| Benajes et al. | The DMDF concept was proposed featuring | • The DMDF concept can fulfill the EURO |

| | | |
|---|---|---|
| [15] (2017) | that the combustion strategy changes as engine load increases.<br>• At low loads with the indicated mean effective pressure (IMEP) lower than 8 bar, a fully premixed RCCI strategy is employed;<br>• When engine load rises up to 15 bar, the combustion strategy is switched to highly premixed RCCI mode;<br>• At full load operation, the diffusive dual-fuel combustion is employed. | VI $NO_x$ limit up to 14 bar IMEP;<br>• Above 5 bar IMEP, the smoke emissions exceed the EURO VI standards for diesel engines, but the majority of the engine map can fulfill the smoke levels below 1 FSN. |
| Benajes et al. [16] (2018) | Comparison of the performance and emissions of two dual-mode combustion concepts over different driving cycles using different fuel combinations. | The dual-mode concept has a potential to be implemented in flexible-fuel engines. |
| García et al. [17] (2019) | Investigation of the effects of the octane number of the low-reactivity fuel at representative operating conditions over the DMDF engine map. | The characteristics of the low-reactivity fuel in the DMDF concept have a major impact on the combustion evolution in a wide range of engine load, speed, low-reactivity fuel fraction, dilution level, and combustion regime. |
| Macián et al. [18] (2019) | Investigation of the effect of the low-pressure exhaust gas recirculation (LP-EGR) on the gaseous and particle emissions of the DMDF concept fueled with standard gasoline and diesel. | • In the fully premixed RCCI mode, the application of the LP-EGR results in high hydrocarbon (HC) and carbon monoxide (CO) emissions;<br>• For the other combustion modes in the DMDF concept, a reduction of the analyzed pollutants is demonstrated with the employment of the LP-EGR compared with the CDC mode. |
| Xu et al. [19] (2020) | Optimization of the operating parameters related to the intake condition and fuel injection strategy for strengthening the engine performance of the DMDF concept fueled with gasoline and diesel fuel at various load conditions. | Gross indicated thermal efficiency above 45% is achieved, and the $NO_x$ and soot emission can be maintained under the Euro VI standard for the whole load range. |
| García et al. [20] (2020) | Exploring the feasibility of using the fuel blend of oxymethylene ether ($OME_x$) and diesel as the high-reactivity fuel instead of pure diesel in the DMDF concept for reducing the | The $OME_x$-diesel blends with an $OME_x$ mass content greater than 70% are able to meet the Euro VI $NO_x$ standard with ultra-low soot levels (< 0.01 g/kWh) up to 80% engine load. |

| | | |
|---|---|---|
| | lifecycle $CO_2$ emission. | |
| García et al.<br>[21]<br>(2020) | Exploration of suitable injector configuration and fuel injection strategy for the DMDF concept with diesel and $OME_x$ respectively as the high-reactivity fuels. | • The long injection durations of $OME_x$ resulted from its low lower heating value is handled with the employment of the injectors with higher flow rate capacity.<br>• The trade-off relationship between engine-out emissions and the mixing capacity of the injection system is solved, while the engine performance is not significantly affected. |

Up to date, the DMDF strategy demonstrates superior advantages for balancing load extension and performance improvement. It has been recognized as a promising dual-fuel combustion concept to satisfy future fuel consumption and emission regulations [17]. However, for the current DMDF strategy, there still exist some aspects to be further improved, among which the piston bowl geometry optimization is the most urgent. At present, the piston bowl geometry for the DMDF strategy is empirically determined. It is well known that the piston bowl geometry can exert significant influences on engine performance. Moreover, the interactions between the piston bowl structure and the injection event are crucial for the fuel/air mixture formation and combustion event for the dual-fuel combustion mode. Thus, the combined optimization of the piston bowl shape with the fuel injection parameters is needed to further enhance the DMDF combustion characteristics.

Up to now, many investigations have been conducted for studying the effects of the piston bowl geometry and searching for the optimal bowl shape for the engines with advanced combustion concepts. Dempsey et al. [22] compared the traditional re-entrant type with a modified shallow type piston based on an RCCI engine fueled with different fuel combinations. It was concluded that the shallow type piston yields better engine efficiency due to lower heat transfer losses. Similar results were also reported by Park et al. [23] that the shallow type piston bowl can contribute to a 35% improvement of the gross indicated thermal efficiency. Xu et al. [24] performed an investigation to study the joint effects of the bowl shape and injection timing based on the partially premixed combustion (PPC) mode and homogeneous charge compression ignition (HCCI) mode. The results indicated that the piston with a stepped-lip shape is favorable for solving the low-load cold start problem in terms of decreasing the intake temperature requirement, which is owing to the fact that the fuel-rich regions can be produced in the stepped-lip piston bowl. Moreover, it was found that the effect of spray/wall interaction is important when the combustion mode shifts from HCCI to PPC. Nazemian et al. [25] optimized the piston bowl geometry of an RCCI engine by utilizing CONVERGE software combined with the design of experiment (DOE) method based on the second law of thermodynamics, and the effects of the main piston bowl shape parameters, including the piston bowl sizes, pip height, and top land height on exergy destruction were discussed. It was reported that the influence of the bowl diameter and bowl depth were the most significant of the exhaust heat recovery. The optimization study performed by Lee et al. [26] indicated that a 9% improvement of fuel consumption with simultaneously reduced $NO_x$ and soot emissions can be attained with a shallow type piston bowl and a narrow injection angle for a gasoline/diesel dual-fuel engine.

From the above literature review, it is confirmed that further optimization of the piston bowl shape used for the DMDF strategy can lead to potential improvements in fuel efficiency and engine-out emissions. Moreover, up to date, there have been few studies reporting the piston bowl geometry optimization over a wide load range for the engines with advanced combustion modes. Thus, in this study, the combined optimization of the piston bowl shape parameters with the fuel injection strategy was conducted over a wide load range for the DMDF mode based on an improved genetic algorithm integrated with the computational fluid dynamics (CFD) simulation. Then, the optimal piston bowl shape coupled with the injection strategy was summarized at different loads. Furthermore, a correlation analysis was conducted to investigate the sensitivity of engine performance to the geometric parameters and injection parameters, which can guide the engine structure design.

# 2. Computational Method

## 2.1. Generation of the Piston bowl geometry and computational mesh

In this study, the shape of the piston bowl is generally described using two straight lines (*i.e.*, Line 1 and Line 2) and three circle curves (*i.e.*, Curve 1, Curve 2, and Curve 3) according to the work of Badra et al. [27]. The straight lines and circle curves are represented by the blue and red lines respectively in Fig. 1. It is comprehensible that the shape is determined by the location of circles A, B, and C, as well as their common tangent lines. Thus, the controllable parameters contain the *X* and *Z* locations of the circle center points A, B, and C, as well as the radius of the three circles, *i.e.*, $R_a$, $R_b$, and $R_c$. Compared with the traditional method, in which the piston bowl shape is described by the Bezier Curve, the control variables are simplified, and the variable number is cut down to seven with this method. In general, once the coordinates and the radius of the three circles are confirmed, the angles of $\alpha$ and $\theta$ (see Fig. 1) can be determined. Thus, the point number and the coordinates of every single point on the piston bowl shape line can be determined, and the piston bowl geometry can be described.

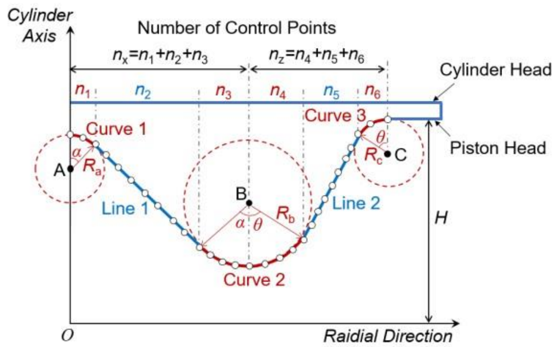


Fig. 1. Illustration of automatic generation of the piston bowl geometry.

The common piston bowl geometries widely used in previous studies for advanced combustion modes, including the Open, Re-entrant, and Shallow piston bowl geometries, can be established using this method, as shown in Fig. 2. Because the bowl shape is specifically determined by the size and location relationship of the three control circles, it can be flexibly controlled by the variables shown in Fig. 1 for the optimization of the bowl shape. Fig. 3 illustrates the computational mesh generation process. In this study, the computational mesh is generated using the pre-processing tool for mesh establishment in the KIVA code. The input file for the pre-processing program is integrated with the geometry generation code according to the shape input file, which includes the information of the three control circles (*i.e.*, circles A, B, and C). Among various generated meshes, the computational sector meshes of three typical piston bowl geometries with the geometric compression ratio of 14.4 are shown in Fig. 2. It can be seen that the computational sector meshes for the Open, Re-entrant, and Shallow piston bowls can be well generated.

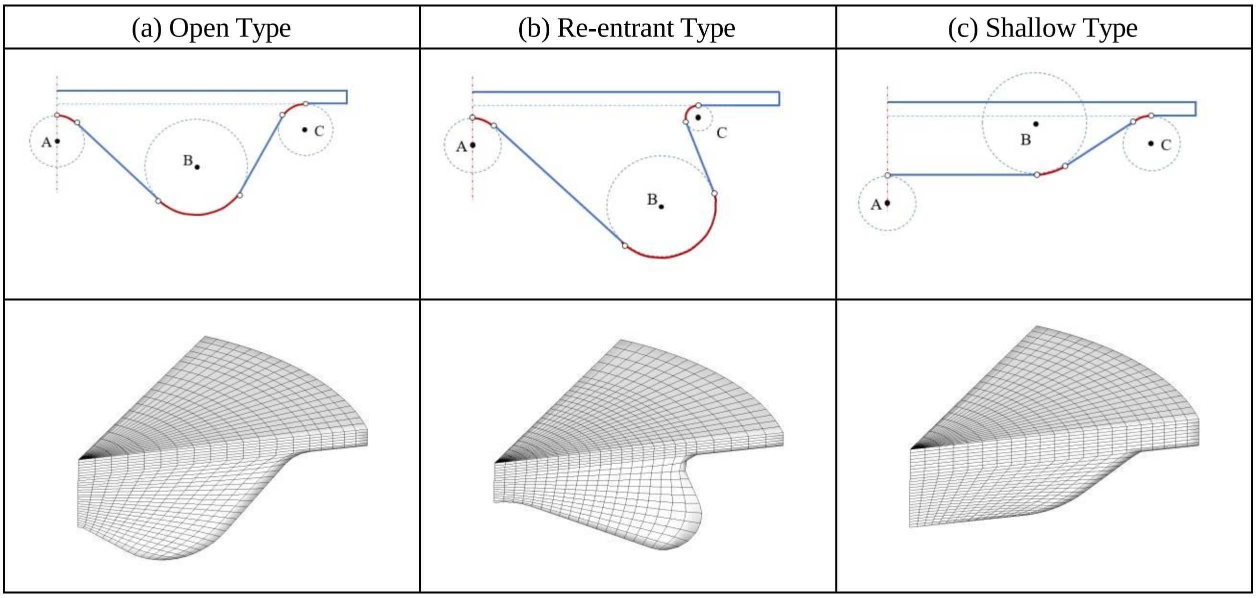


Fig. 2. Common piston bowl types and corresponding computational meshes at top dead center.

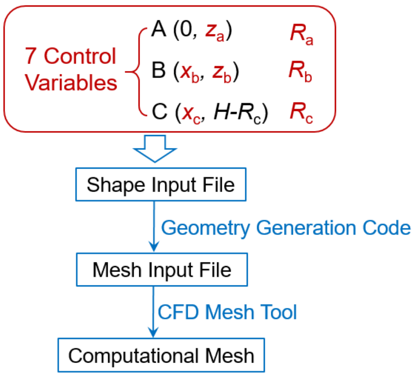


Fig. 3. Computational mesh generation procedure.

## 2.2. CFD Model

The CFD calculation of this study was conducted using the open-source KIVA-3V code [28] for simulating the engine working process. Based on the framework of KIVA-3V, several improvements and updates about the sub-models have been performed. The turbulence model improved by Wang et al. [29] was used for modeling the in-cylinder flow. The improved models were used for modeling the spray impingement [30] and liquid film evolution processes [31]. Moreover, the quasi-dimensional model for describing the vaporization processes of fuel droplets [32] and liquid films [33] was integrated. Meanwhile, the wall heat transfer model [34], droplet collision model [35], and droplet breakup model [36] were also contained in this CFD code. For dealing with the fuel chemistry, the KIVA-3V code was coupled with the CHEMKIN solver [37]. Furthermore, the skeletal chemical mechanism constructed by Chang et al. [38] was used for predicting the ignition and combustion characteristics of the fuel blends. The diesel and gasoline fuel were represented by *n*-heptane and *iso*-octane, respectively. It should be noted that the above models have been validated based on numerous experimental data in the previous works, e.g., Refs. [39, 40].

Table 2. Engine specifications

| | |
|---|---|
| Bore (mm) | 110.0 |
| Stroke (mm) | 135.0 |
| Connecting rod length (mm) | 212.5 |
| Original compression ratio | 14.4:1 |
| Swirl Ratio | 2.3 |
| Direct fuel injection system | Common rail |
| Number of nozzle holes | 7 |
| Spray angle (°) | 75.0 |
| Nozzle hole diameter (mm) | 0.177 |

The computational model was validated ahead of the optimization study. Table 2 lists the detailed information of the engine tested in this work. The validation was performed at a constant engine speed of 1200 rev/min with different IMEP. Table 3 lists the basic conditions and the operating parameters of the validation cases. Table 4 lists the the properties of the diesel and gasoline fuels tested in the experiment [15]. Fig. 4 illustrates the computational mesh for the original DMDF combustion chamber, and the mesh is generated using the method mentioned above. Fig. 5 illustrates the comparison of the simulated and experimental in-cylinder pressure and heat release rate (HRR) traces for five test cases with different IMEP. The comparison results show that the simulated traces can well match with the measurements of Benajes et al. [15]. This indicates that the simulation with the generated computational mesh can accurately reproduce the combustion process of the DMDF mode at different loads.

Table 3. Basic conditions of the validation cases.

| IMEP (bar) | 5.9 | 9.9 | 11.9 | 17.3 | 22.6 |
|---|---|---|---|---|---|
| $p_{ivc}$ (bar) | 1.60 | 2.29 | 2.32 | 3.01 | 3.09 |
| $T_{ivc}$ (K) | 332.6 | 329.1 | 347.9 | 332.2 | 356.1 |
| EGR rate (%) | 19.7 | 55.5 | 50.2 | 45.1 | 31.0 |
| SOI1 (°CAATDC) | -48.0 | -50.0 | -45.0 | - | - |
| SOI2 (°CAATDC) | -41.9 | -4.4 | -5.0 | 0.0 | 6.0 |
| Total fuel flow (mg/cycle) | 35.5 | 65.2 | 81.1 | 116.9 | 145.3 |
| Diesel flow (mg/cycle) | 31.8 | 62.3 | 50.4 | 52.9 | 49.3 |
| Gasoline flow (mg/cycle) | 3.7 | 2.9 | 30.7 | 64.0 | 96.0 |

Table 4. Properties of the diesel and gasoline fuels

| | Diesel | Gasoline |
|---|---|---|
| Density (kg/m$^3$) @ T=288.15 K | 824 | 720 |
| Viscosity (mm$^2$/s) @ T=313.15 K | 2.8 | - |
| Research Octane Number (-) | - | 95 |
| Motor Octane Number (-) | - | 85 |
| Cetane Number (-) | 51 | - |
| Lower Heating Value (kJ/kg) | 42.92 | 42.40 |

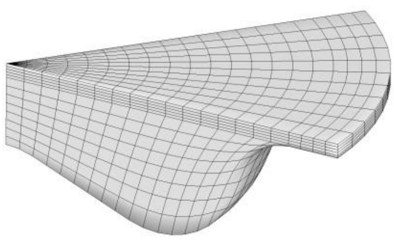

Fig. 4. Computational mesh for the original DMDF combustion chamber.

Fig. 6 shows comparisons of HC, CO, $NO_x$ and soot emissions between simulation and experiment. It is found that the overall variation trend with varying IMEP can be well captured for the four emissions. However, the discrepancies in magnitude still exist between the simulated and experimental emission levels. This is primarily owing to the complexity of the in-cylinder flow and fuel/air mixing process, the imperfection of the chemical mechanism [41], and the measurement uncertainties [3]. Since the main task of the simulation tool of this study can be qualified by the capability of predicting the emission variation trend as a specific operating parameter changes, the computational model and mesh can be employed for the optimization study in the following work.

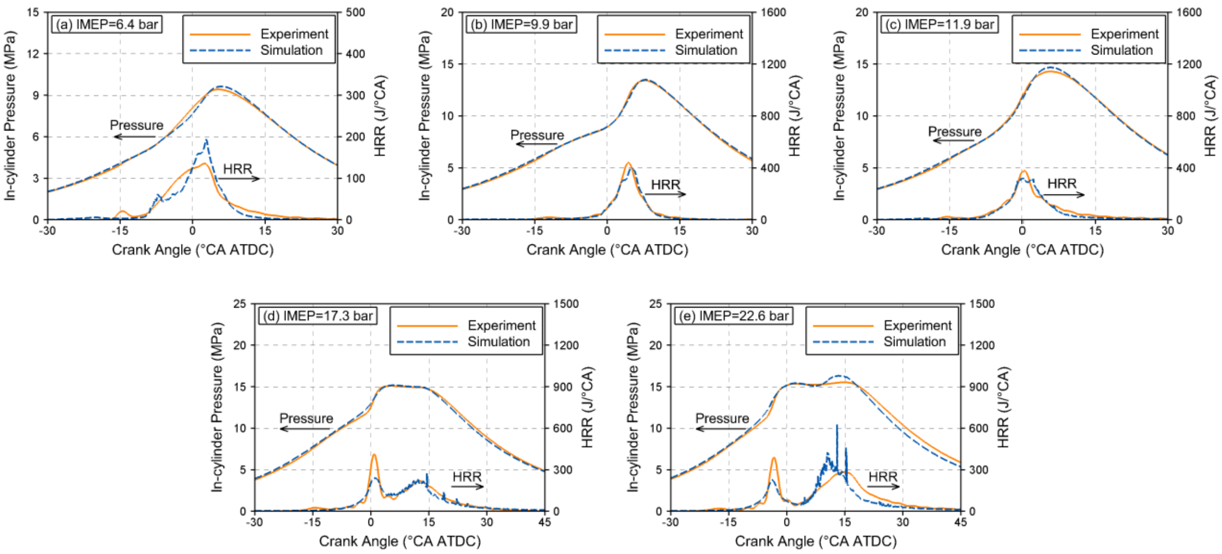


Fig. 5. Validations of the pressure and HRR at different loads.

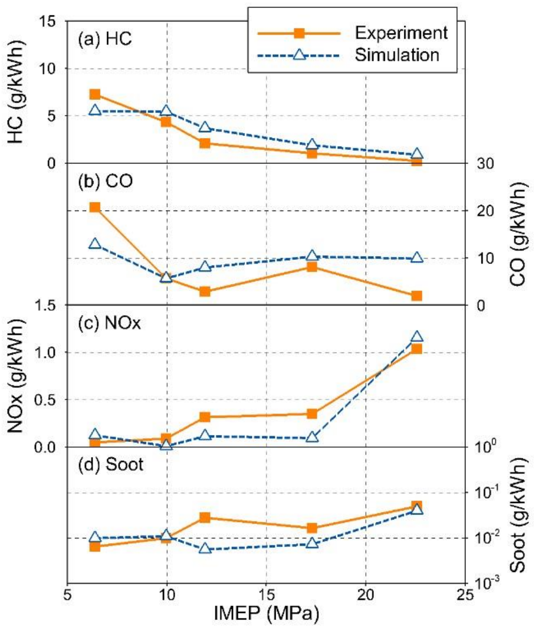


Fig. 6. Validations of the emissions at different loads.

## 2.3. Optimization method

In this study, the optimization of the piston bowl geometry coupled with the injection strategy involves a considerable number of variables. In order to realize the multi-variable multi-objective optimization and simultaneously minimize the fuel consumption and engine-out emissions, the non-dominated sorting genetic algorithm II (NSGA-II) [42] was utilized. The flowchart of the optimization procedure is illustrated in Fig. 7. The global numerical system contains two parts, *i.e.*, the optimization part using GA and the CFD part using KIVA. The GA code is coupled with the KIVA code containing the geometry generation code. In the optimization calculation, the GA code generates the shape input and CFD input files. The geometry generation code is in charge of exporting the mesh input file, which is the input file for the meshing program to create the computational mesh. CFD calculation is performed with the CFD input file and the computational mesh. GA code analyzes the CFD calculation results of each citizen and generates new data for the next generation calculation.

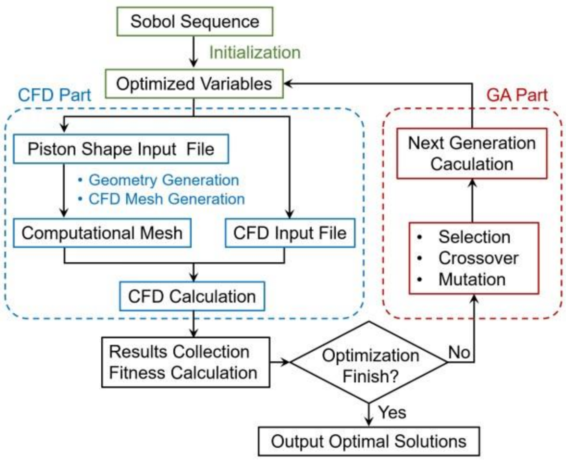


Fig. 7. Illustration of the optimization computation process.

Considering the increased number of variables, the initial population size needs to be enlarged to keep the diversity of the optimal solutions in the GA calculation. In this study, the initialization of the citizens for the first generation is improved by introducing the Sobol sequence sampling method [43] instead of the traditional random sampling method used in NSGA-II. Fig. 8 shows the distributions of the random samples and Sobol samples with a constant sample number of 250 in a two-dimensional variable coordinate. It can be found that the distribution of the Sobol samples is more uniform than that of the random samples. This indicates that the Sobol sequence sampling method can provide a better uniformity for the multi-dimensional variables by sufficiently covering the whole variation ranges of the variables under the conditions with limited population size. Therefore, the introduction of the Sobol sequence sampling method in this study is aiming at including more possible cases and searching for the global optimal solutions more effectively, and a relatively small population size can be utilized simultaneously for saving computational resources.

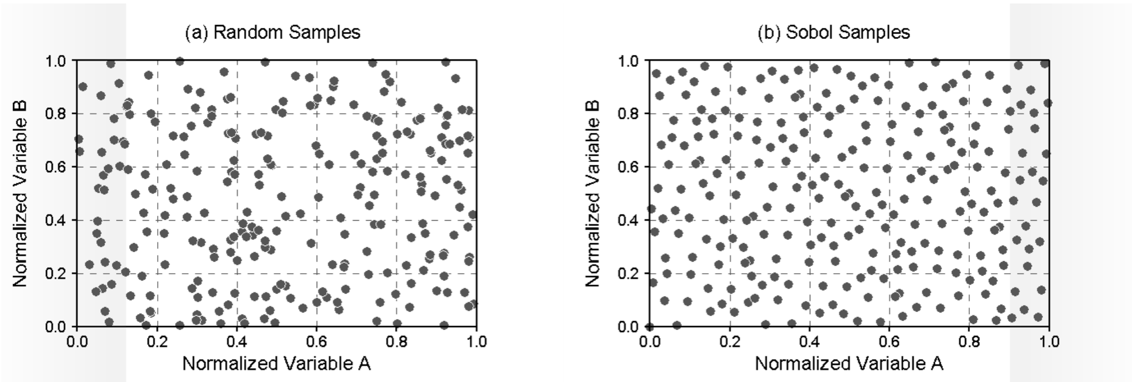


Fig. 8. Comparison of random samples and Sobol samples.

# 3. Results and Discussion

## 3.1. Global optimization results

In a previous study from the authors [19], based on the diesel/gasoline DMDF combustion concept, the operating parameters related to the injection strategy and the air intake conditions were optimized to enhance the engine performance (*i.e.*, Step 1 optimization). A total of seven operating parameters with crucial influences were chosen as the variables at three different loads in the previous study. Since the injection/wall interaction plays a critical role in the fuel/air mixture formation, the optimization of the injection parameters cooperated with the piston bowl geometry was further conducted at different load conditions in this study (*i.e.*, Step 2 optimization). The aim is to search for the most suitable piston bowl shape for the DMDF combustion mode over a wide load range. A total of 14 parameters were considered in the present work, including seven geometric parameters and seven engine operating parameters. The optimization specifications are listed in Table 5.

Table 5. Optimization specifications

| | Parameter | Range |
|---|---|---|
| Variables | Premix Ratio | (0.0, 1.0) |
| | SOI1 (°CA ATDC) | (-80.0, 10.0) |
| | SOI2 (°CA ATDC) | (SOI1, 10.0) |
| | MF1 | (0.0, 1.0) |
| | Spray angle (°) | (15, 85) |
| | Injection Pressure (MPa) | (50, 180) |
| | Compression Ratio | (12.0, 18.0) |
| | Normalized $Z_a$ | (0.0, 1.0) |
| | Normalized $Z_b$ | (0.0, 1.0) |
| | Normalized $X_b$ | (0.0, 1.0) |
| | Normalized $X_c$ | (0.0, 1.0) |
| | Normalized $R_a$ | (0.0, 1.0) |
| | Normalized $R_b$ | (0.0, 1.0) |
| | Normalized $R_c$ | (0.0, 1.0) |
| Constraints | EISFC (g/kWh) | <250.0 |
| | $T_{max}$ (K) | >1100.0 |
| | $NO_x$ (g/kWh) | <0.4 |
| | soot (g/kWh) | <0.01 |
| | PPRR (bar/°CA) | <15.0 |
| | $p_{max}$ (MPa) | <20.0 |
| | RI (MW/m$^2$) | <10.0 |

Table 6. Initial conditions at IVC timing at each load.

| | Low | Mid | High |
|---|---|---|---|
| $p_{ivc}$ (bar) | 1.51 | 1.99 | 3.30 |
| $T_{ivc}$ (K) | 392.2 | 306.1 | 315.5 |
| EGR (%) | 6.5 | 6.5 | 31.0 |

The seven geometric parameters are normalized $Z_a$, $Z_b$, $X_b$, $X_c$, $R_a$, $R_b$, and $R_c$, which determine the piston bowl shape, as illustrated in Figs. 1 and 2. The variation ranges of the geometric parameters are all from 0.0 to 1.0. The operating parameters relating to the direct fuel injection event include the two injection timings (*i.e.*, SOI1 and SOI2), injection pressure (*i.e.*, $p_{inj}$), mass fraction of the first injection (*i.e.*, MF1), and spray angle (SA). The variation ranges of the injection parameters can be found in Table 5. The SA is equal to a half of the injection plume included angle. Moreover, the premix ratio (*i.e.*, PR) of gasoline fuel and geometric compression ratio (*i.e.*, GCR) were also included in the variables to be optimized. In the engine simulations, the squish height was adjusted to match the desired GCR.

During the optimization process, the equivalent indicated specific fuel consumption (EISFC), $NO_x$, and soot emissions are selected as the objectives to urge the populations into the pleasant fuel economy and low-emission orientation. Meanwhile, several constraints are taken into consideration in order to guarantee the rationality of the optimal cases. In the optimization calculation, the peak in-cylinder temperature is kept above 1100 K to avoid misfire. For forbidding rough engine operations, the maximum in-cylinder pressure ($p_{max}$), ringing intensity (RI), and PPRR are limited under 19.0 MPa, 10 MW/m$^2$, and 15.0 bar/°CA, respectively [15]. The EISFC is restricted under 250 g/kWh to ensure satisfactory fuel economy, while the $NO_x$ and soot emission limits are set according to the Euro VI regulations (*i.e.*, 0.4 and 0.01 g/kWh, respectively). Moreover, the operating loads for optimization are located at 5.9, 11.9, and 22.6 bar, which are chosen from the baseline cases validated in Section 2.2. According to our previous study, the optimized air intake conditions including the initial temperature ($T_{ivc}$) and pressure ($p_{ivc}$) at IVC timing, as well as the EGR rate, are used in this work. Table 6 lists the setup of the initial conditions at the IVC timing for the optimization calculation at the three loads.

The optimization results of the present study are first compared with the previous optimization results to demonstrate the improvements gained from the piston bowl geometry optimization. Fig. 9 shows the evolution of the EISFC and $NO_x$ emissions for all the generated cases in the population at the various loads. The yellow and blue symbols represent the generated cases in the previous optimization (*i.e.*, Step 1 optimization) and the present optimization (*i.e.*, Step 2 optimization), respectively. Each case is colored by the generation number. A deeper color denotes a higher optimization degree. From the comparison of the Step 1 optimization to the Step 2 optimization, it can be found that EISFC is further decreased after the piston bowl geometry optimization while $NO_x$ emissions can still meet the Euro VI limit. The soot emissions of the optimal cases (*i.e.*, the deeper-color symbols) are also below the Euro VI limit, which is not illustrated in Fig. 9 due to space limitation. This well demonstrates the improvement of fuel economy without sacrificing the engine-out emissions in the Step 2 optimization. Overall, the above results indicate that the piston bowl geometry optimization further enhances the performance of the DMDF combustion mode at different loads.

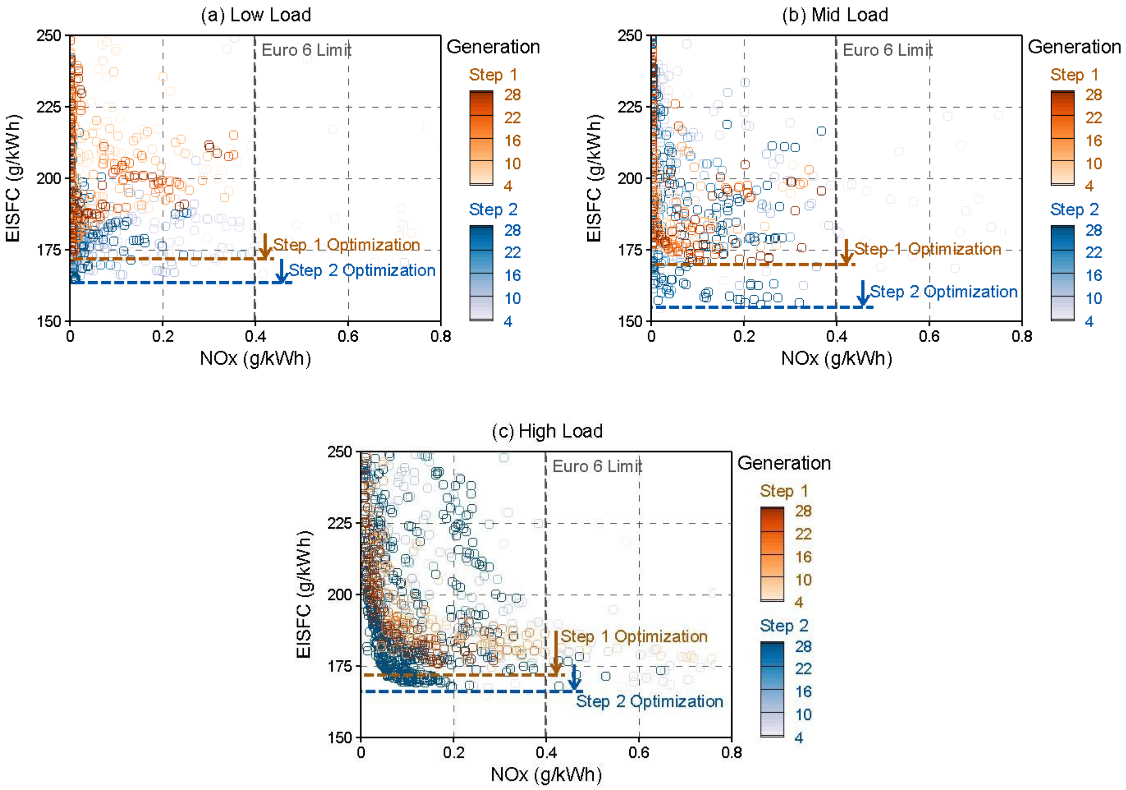


Fig. 9. Evolution of the EISFC and $NO_x$ emissions during the optimization at different loads.

Fig. 10 shows the comparison of the piston bowl shapes obtained during the optimization process at different loads. The dashed black line represents the baseline piston bowl shape for the DMDF mode [15]. The dashed grey line represents the top dead center position. The solid grey lines denote all the piston bowl profiles generated from the genetic algorithm. In this section, the cases with competitive fuel efficiency while meeting the Euro VI standards of the $NO_x$ and soot emissions are chosen as the optimal cases at each load. Furthermore, in order to provide more options for the DMDF piston bowl geometry design, among the optimal piston bowls, two typical shapes with distinguishing geometric characteristics are picked up to represent the optimal piston geometry at each load. The selected optimal cases are named as Low-A and Low-B for low load, Mid-A and Mid-B for mid load, and High-A and High-B for high load. As shown in Fig. 10, the optimal shapes are represented by the orange and blue lines.

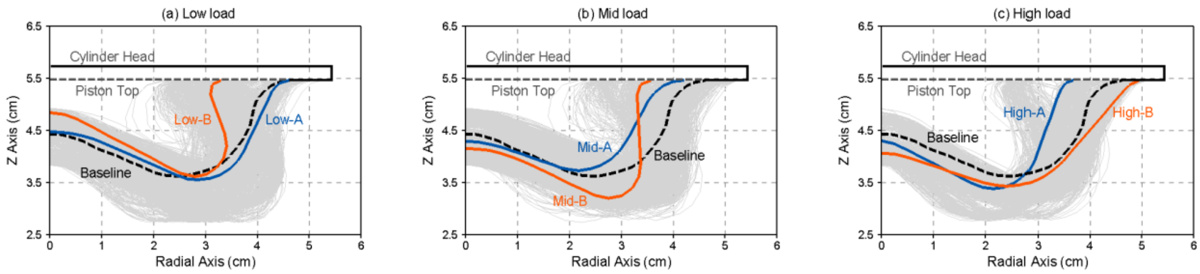


Fig. 10 Generated piston bowl shapes and typical optimal piston bowl shapes in the optimization at different loads.

It is seen from Fig. 10 that the optimal bowl geometries at low and mid loads contain both the open type and re-entrant type bowl, whereas the high load only contains the open type bowl. At low load, the optimal re-entrant type bowl (*i.e.*, case Low-B) features a smaller bowl width, while the optimal open type piston bowl (*i.e.*, case Low-A) features a similar bowl width compared with the baseline piston bowl, as shown in Fig. 10(a). At mid load, the optimal open type piston bowl (*i.e.*, case Mid-A) characterizes a relatively larger bowl width and smaller bowl depth, while the optimal re-entrant type bowl (*i.e.*, case Mid-B) characterizes a relatively smaller bowl width and larger bowl depth, as shown in Fig. 10(b). At high load, the two optimal cases feature a smaller bowl width (*i.e.*, case High-A) and a larger bowl width (*i.e.*, case High-B), respectively. Meanwhile, both of the two optimal cases at high load exhibit larger bowl depth compared with the baseline piston geometry, as shown in Fig. 10(c).

In order to demonstrate the engine improvements using the optimal piston bowl shapes, the optimal cases are compared to the previous optimal cases and the baseline cases in terms of fuel efficiency, $NO_x$ and soot emissions, as shown in Fig. 11. The grey bars and symbols represent the baseline cases and the optimal cases from the previous optimization (*i.e.*, Step 1 optimization). The orange and blue bars and symbols represent the optimal cases from the piston bowl geometry optimization (*i.e.*, Step 2 optimization). The left figures illustrate the comparisons of thermal efficiency, and the right figures provide the comparisons for $NO_x$ and soot emissions. As depicted in the left sub-figures of Fig. 11, significant improvement can be found for the thermal efficiency with the previous optimization (*i.e.*, Step 1) at the three loads. After optimizing the piston bowl shape combined with the injection parameters (*i.e.*, Step 2), the thermal efficiency is further improved. The thermal efficiency is increased up to 1.4%, 4.4%, and 1.4% for the low, mid, and high loads, respectively. It is worth noting that an indicated thermal efficiency up to 51.8% can be realized at mid load with the combined optimization. This well demonstrates the benefit gained for fuel economy from the piston bowl geometry optimization.

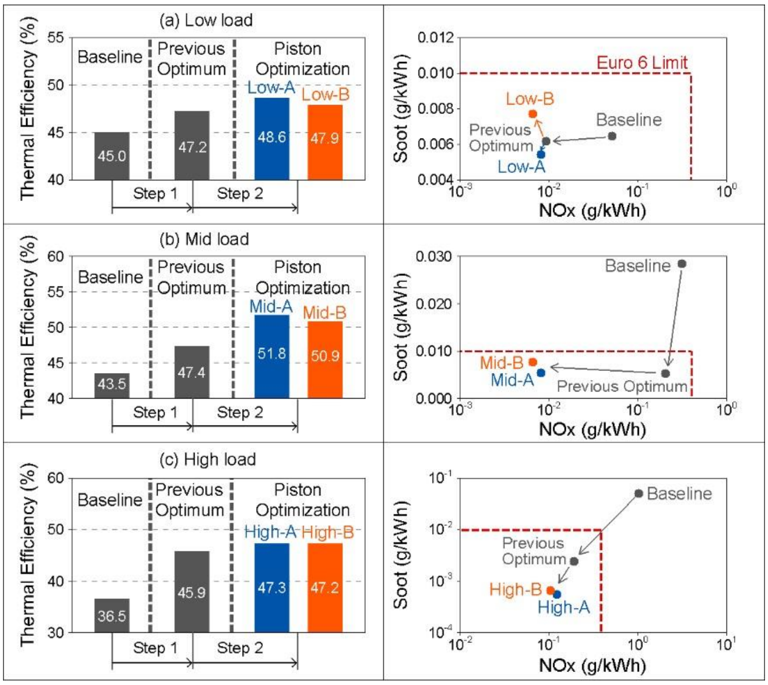


Fig. 11. Comparisons of thermal efficiency, $NO_x$ emissions, and soot emissions among the baseline cases and the optimal cases in Step 1 and Step 2 optimizations.

As for the right sub-figures of Fig. 11, both the $NO_x$ and soot emissions are continuously decreased after Step 1 and Step 2 optimizations at high load. At low and mid loads, the improvements of $NO_x$ and soot emissions for Step 2 optimization are not as significant as those for Step 1 optimization, but either $NO_x$ or soot emissions can still be further decreased to some extent after Step 2 optimization compared to the cases of Step 1 optimization. For both the optimal cases, the $NO_x$ and soot emissions can meet the Euro VI limits. Thus, it is concluded that the thermal efficiency can be significantly improved with the piston bowl geometry optimization without sacrificing $NO_x$ and soot emissions.

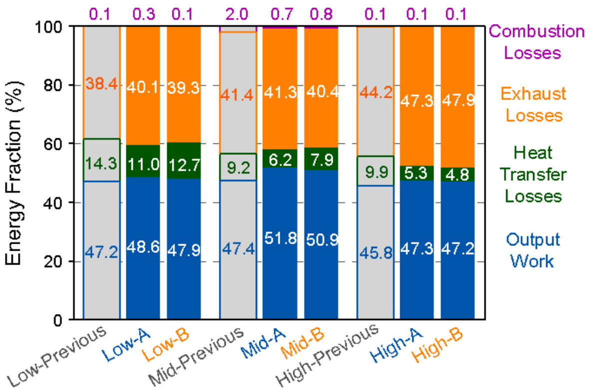


Fig. 12. Illustration of the energy fractions of optimal cases and baseline cases.

Furthermore, the energy analysis was conducted for investigating fuel efficiency benefits. As illustrated in Fig. 12, the energy fractions of the optimal cases in Step 2 optimization are compared with those of the previous optimal cases in Step 1 optimization. The bar colored by grey represents the previous optimal case while the other two represent the optimal cases from the piston bowl geometry optimization at each load. According to the first law of thermodynamics, the total input fuel energy is transferred into four parts during the combustion process, including output work, heat transfer losses, exhaust losses, and incomplete combustion (*i.e.*, combustion losses), as shown in Fig. 12. It is noted that the energy fraction of output work is directly related to the thermal efficiency depicted in Fig. 11. It can be seen from Fig. 12 that the purple bars are not obviously visible, which is due to the fact that the combustion losses are relatively low (less than 1%) under the whole load range. This is because that a majority of HC and CO emissions are reduced by the oxidation reactions in the late combustion stage. Thus, the engine-out emission levels of HC and CO are low. From the comparison of the optimal cases from the piston bowl geometry optimization with those from the previous optimization, it can be found that the improvement of the output work (*i.e.*, thermal efficiency) is mainly resulted from the decrease of the heat transfer losses at low and high loads. At mid load, the decreases of both the heat transfer losses and combustion losses contribute to the improvement of output work. This demonstrates the benefits of thermal efficiency gained from the piston bowl geometry optimization.

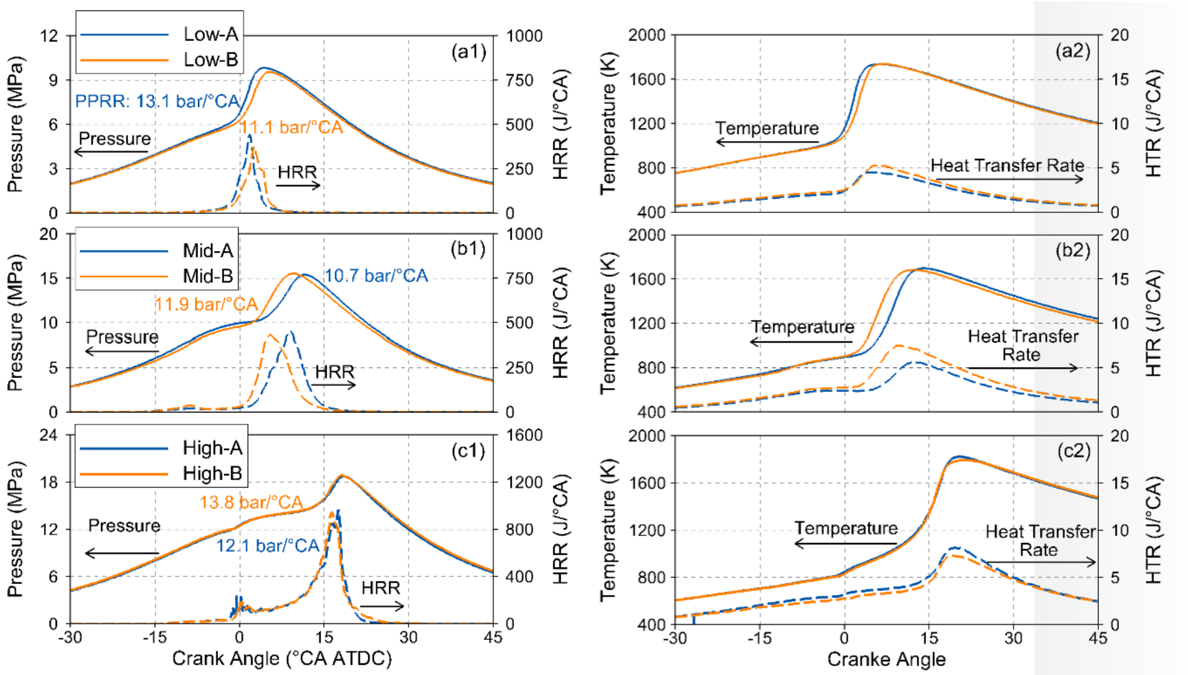


Fig. 13. Comparison of the in-cylinder pressure, HRR, temperature, and heat transfer rate (HTR) traces between the optimal cases.

Furthermore, the combustion process of the optimal cases is analyzed in detail for further explaining the improved performance after the piston bowl geometry optimization. Fig. 13 depicts the in-cylinder pressure, temperature, HRR, and heat transfer rate (HTR) traces of the optimal cases. Overall, from the comparisons of the pressure, temperature, and HRR, it is found that the traces at each load are very similar, especially for the high load condition, in spite of slight differences existing in the combustion phasing between the different optimal cases. This indicates that the different optimal cases exhibits similar combustion characteristics at each load. In terms of the comparison of the three loads, the combustion phasing is found to be retarded with increasing load, which is consistent with previous results [11, 19]. This is mainly aiming at controlling ringing intensity and preventing the engine knock. It can be seen from the denoted PPRR in Fig. 13 that at mid and high loads, by managing the combustion process and combustion phasing, the PPRR can meet the limit of 15 bar/°CA. At low load, although a relatively advanced combustion phasing is presented, the PPRR is still under the limit since the released fuel energy is much lower than those of mid and high loads.

Moreover, in order to understand the heat transfer process, the heat transfer rate (HTR) traces of the optimal cases at each load are also illustrated in Fig. 13. By comparing the HTR traces at each load, the differences in the heat transfer losses (see Fig. 12) can be explained. It can be found that the global HTR of cases Low-B, Mid-B, and High-A is higher than that of cases Low-A, Mid-A, and High-B, respectively. Thus, the heat transfer losses of cases Low-B, Mid-B, and High-A are relatively higher. However, the heat transfer process cannot be simply explained by the evolution of the global in-cylinder temperature since the piston bowl geometry and the combustion occurrence location also play critical roles. Thus, this will be explained in the following section.

## 3.2. Typical optimal piston bowl geometry and corresponding injection strategy

In this section, the optimal piston bowl shape coupled with the corresponding fuel injection strategy is summarized at each load. Table 7 lists the operating parameters of each optimal cases. Meanwhile, the fuel injection event and the fuel/air mixture formation process are analyzed as well. Fig. 14 shows the liquid fuel distribution after injection timing and the equivalence ratio distribution before ignition for cases Low-A and Low-B. As mentioned above, the optimal bowl shape for case Low-A is open type, while the optimal bowl shape for case Low-B is re-entrant type. Besides, as listed in Table 7, both of the two optimal cases utilize a similar compression ratio with that of the original engine setup (*i.e.*, 14.4) [15].

Table 7. Operating parameters of the optimal cases.

| | Low-A | Low-B | Mid-A | Mid-B | High-A | High-B |
|---|---|---|---|---|---|---|
| CR | 14.6 | 14.7 | 16.7 | 15.8 | 14.0 | 13.8 |
| PR | 97% | 97% | 90% | 76% | 96% | 96% |
| $p_{inj}$ (MPa) | 167 | 101 | 140 | 162 | 176 | 175 |
| SOI1 (°CA ATDC) | -57 | -51 | -56 | -79 | -28 | -26 |
| SOI2 (°CA ATDC) | - | - | -51 | -60 | -15 | -18 |

As for the fuel injection strategy, only the cases with the single injection strategy are retained in the genetic algorithm optimization at low load. By comparing Figs. 14(a1) and 14(b1), it is found that case Low-A is coupled with a relatively wider spray angle (SA) of 84.6°. In contrast with case Low-A, case Low-B is coupled with a relatively narrower SA of 76.2°, which is similar to that of the original experimental setup (*i.e.*, 75°) [15]. Figs. 14(a2) and 14(b2) illustrate the in-cylinder equivalence ratio distributions before ignition for cases Low-A and Low-B, respectively. From the comparison, it can be found that the high fuel concentration locations of the two cases are similar, which is owing to the combined effects of the piston bowl geometry and the fuel injection event. As can be seen, a stronger tumble flow is organized in the re-entrant piston bowl geometry in contrast to the open type bowl, which is also indicated by Miles and Andersson [44], as well as Lee et al. [45]. This results in larger flow velocity around the cylinder head and the piston wall near top dead center (TDC) for case Low-B. Thus, although a relatively lower injection pressure ($p_{inj}$) and a later SOI timing are employed for case Low-B, the injected fuel can also propagate to the similar location as that of case Low-A.

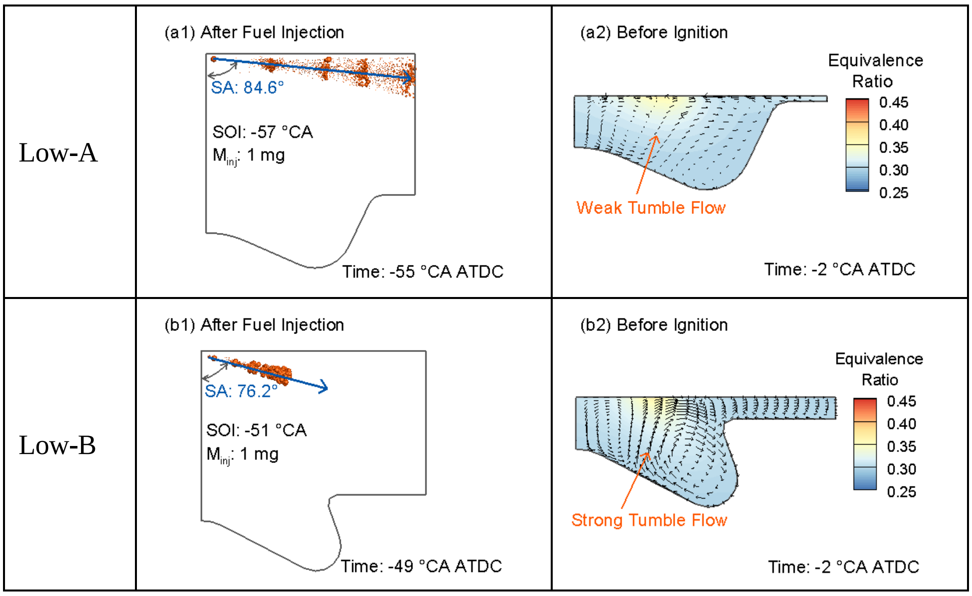


Fig. 14. Illustration of the optimal piston bowl shape, fuel injection and the fuel/air mixture formation at low load.

Fig. 15 depicts the liquid fuel distribution after injection timing and the equivalence ratio distribution before ignition for the optimal cases at mid load (*i.e.*, cases Mid-A and Mid-B). The shallow open piston bowl of case Mid-A is coupled with a relatively wider SA and lower injection pressure, as well as later fuel injection timings. On the contrary, the deep re-entrant piston bowl of case Mid-B is integrated with a relatively narrower SA and higher injection pressure, as well as earlier fuel injection timings. For case Mid-A, due to the lower $p_{inj}$ and wider SA compared to that of case Mid-B, the fuel spray penetration is relatively shorter, and the fuel mainly concentrates near the cylinder head, as shown in Fig. 15(a3), which is similar to the situation at low load. For case Mid-B, owing to the higher $p_{inj}$ and earlier fuel injection timings, the fuel penetration spray is much longer, which takes more fuel into the squish region. However, the strong squish flow in case Mid-B brings most of the injected fuel back into the bowl region, as shown in Fig. 15(b3). Meanwhile, the strong tumble flow resulted from the deep piston bowl geometry is helpful for the fuel/air mixing in case Mid-B with the employment of more injected fuel. Furthermore, as listed in Table 4, relatively higher CRs are employed in cases Mid-A and Mid-B for strengthening fuel efficiency. Thus, a significant improvement in thermal efficiency can be seen in Fig. 11. Meanwhile, with the help of lower initial temperature (see Table 3), the combustion phasing can be well controlled and the PPRR limit is maintained at mid load.

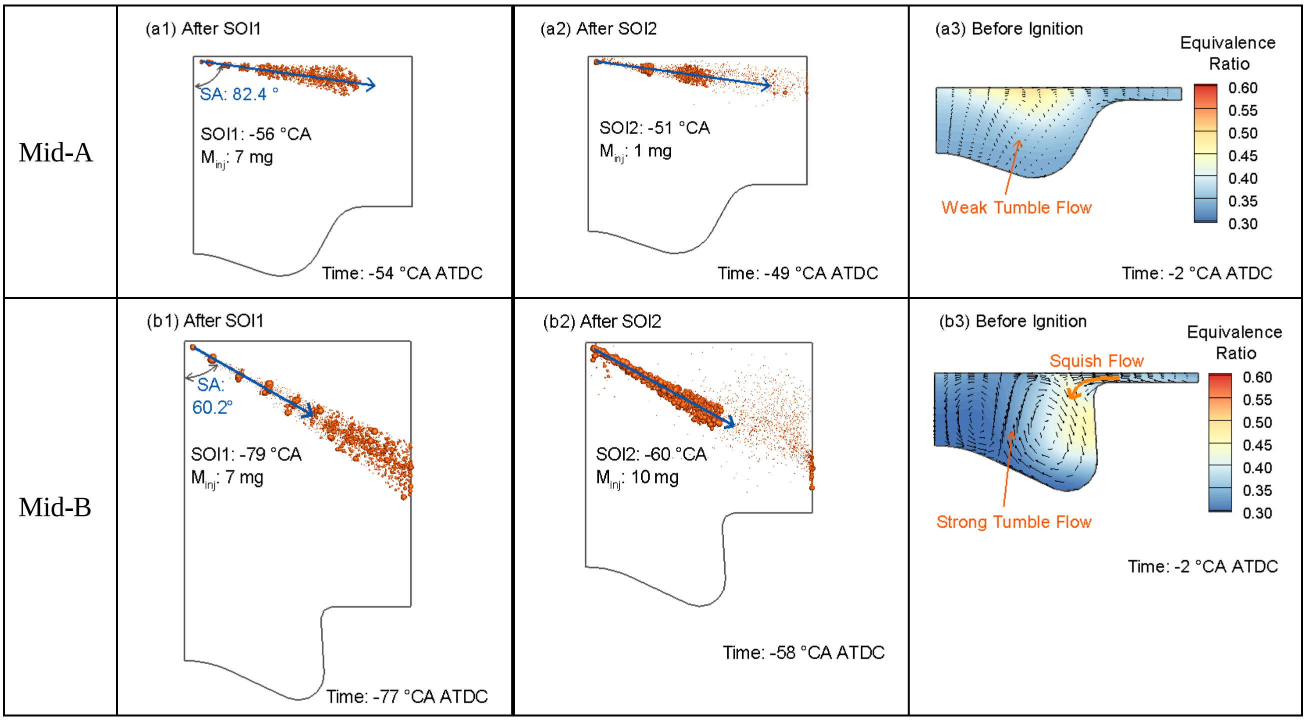


Fig. 15. Illustration of the optimal piston bowl shape, fuel injection and the fuel/air mixture formation at mid load.

As for high load, as shown in Fig. 16, both cases High-A and High-B employ the open type piston bowl. The difference is that case High-A utilizes a deep-narrow bowl geometry, while case High-B employs a shallow-wide open bowl geometry. Moreover, case High-A is coupled with a narrower SA, whereas case High-B uses a wider SA. In terms of fuel injection timings, both of the SOI1 and SOI2 timings of cases High-A and High-B are retarded compared with those of the optimal cases at low and mid loads. This is for avoiding advanced ignition, which can lead to high pressure rise rate and consequently engine knock at high load. Meanwhile, the relatively lower compression ratio employed by cases High-A and High-B (see Table 4) is also beneficial for controlling the PPRR. In such a way, a large fraction of gasoline can be premixed for the DMDF combustion mode at high load without exceeding the PPRR limit. Therefore, as shown in Table 4, the premix ratio of cases High-A and High-B can be increased to an equivalent level as that of mid and low loads. This is helpful for controlling the $NO_x$ and soot emissions owing to the premixed combustion enhancement.

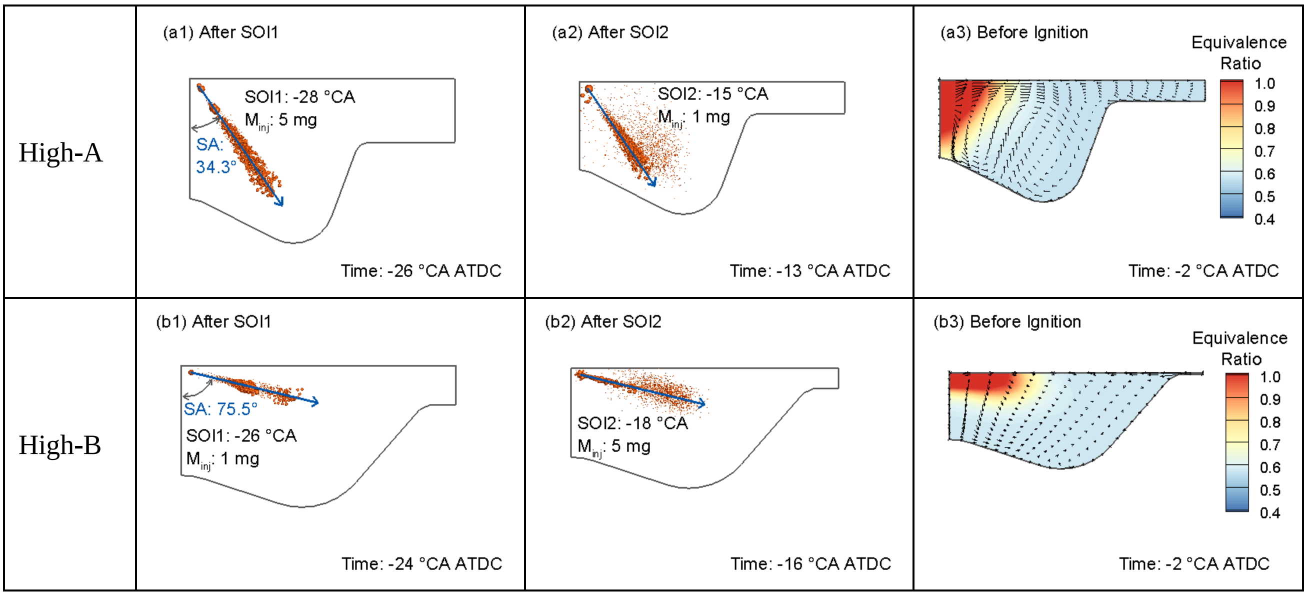


Fig. 16. Illustration of the optimal piston bowl shape, fuel injection and the fuel/air mixture formation at high load.

The late injection timings combined with the less injected fuel mass result in shorter fuel penetrations for cases High-A and High-B. Moreover, although the injection pressure is higher than lower loads (see Table 4), the increasing in-cylinder charge density resulted from the higher intake pressure at high load (see Table 3) restricts the propagation of the injected diesel fuel. Thus, the injected fuel mainly concentrates around the injection nozzle region, as shown in Figs. 16(a3) and 16(b3). Furthermore, from the comparison of the flow field of cases High-A and High-B, it is confirmed again that the deep and narrow bowl geometry can produce strong tumble flow compared with the shallow and wide piston geometry.

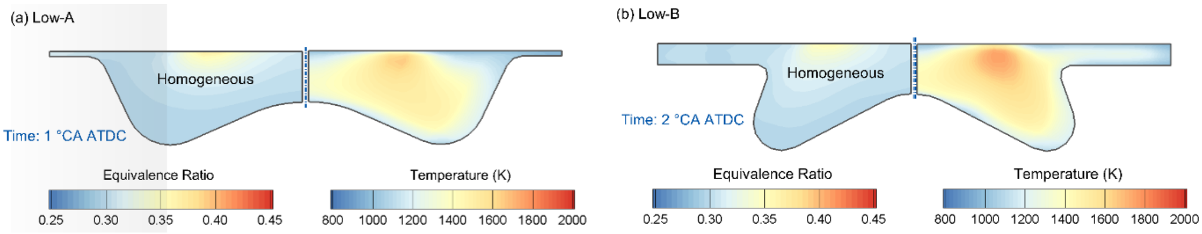


Fig. 17. In-cylinder equivalence ratio and temperature distributions at CA50 for cases Low-A and Low-B.

In order to further investigate the combustion characteristics of the optimal cases, the in-cylinder temperature and equivalence ratio distributions during the combustion process are further analyzed in this section. Figs. 17 to 19 depicts the in-cylinder temperature and equivalence ratio distributions at the time of 50% burning point (CA50) for the optimal cases of low, mid, and high loads, respectively. It can be found that the locations of the high fuel vapor concentration and the combustion occurrence are directly related to the fuel distribution pattern before ignition shown in the above figures, which is determined by the joint effects of piston bowl geometry and fuel injection strategy. As shown in Fig. 17, since the direct-injected fuel mass is lower, and a majority of fuel is premixed in the intake port, both cases Low-A and Low-B exhibit a homogeneous equivalence ratio distribution. This leads to the corresponding homogeneous combustion characteristics for both the optimal cases, which is helpful for the $NO_x$ and soot emission control. This is consistent with the previous results at low load operation [19].

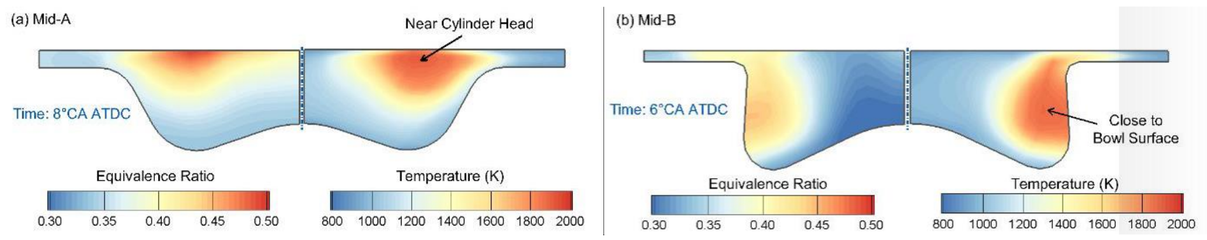


Fig. 18. In-cylinder equivalence ratio and temperature distributions at CA50 for cases Mid-A and Mid-B.

At mid load, with the increase of the injected fuel mass, the local equivalence ratio concentration is increased compared with the low load, as seen in Fig. 18. For case Mid-A, consistently with the low-load optimal cases, a high premix ratio (see Table 4) is utilized for enhancing the premix combustion, leading to pleasant $NO_x$ and soot emissions. For case Mid-B, although a higher direct-injected diesel fuel mass (*i.e.*, lower premix ratio) is employed, the local equivalence ratio concentration is lower than that of case Mid-A. This is because that the optimized deep re-entrant piston bowl geometry of case Mid-B produces a stronger tumble flow within the bowl region, leading to more sufficient premixing of the injected fuel with the in-cylinder charge before the combustion occurs. Thus, the Euro VI emission limits for the $NO_x$ and soot emissions can also be maintained for case Mid-B. Moreover, consistent with the vapor distribution of the direct-injected diesel fuel before ignition (see Fig. 15), the combustion occurrence location is near the cylinder head and close to the bowl surface for case Mid-A and case Mid-B, respectively.

At high load, although the injected mass is not further increased, the local equivalence ratio concentration is considerably elevated for the optimal cases, as illustrated in Fig. 19. This is mainly due to the shorter fuel spray penetration resulted from the later fuel injection timing and the increased in-cylinder charge density. Correspondingly, the combustion occurs near the cylinder axis region, which places the high-temperature region away from the piston bowl surface or the cylinder wall during the combustion phasing.

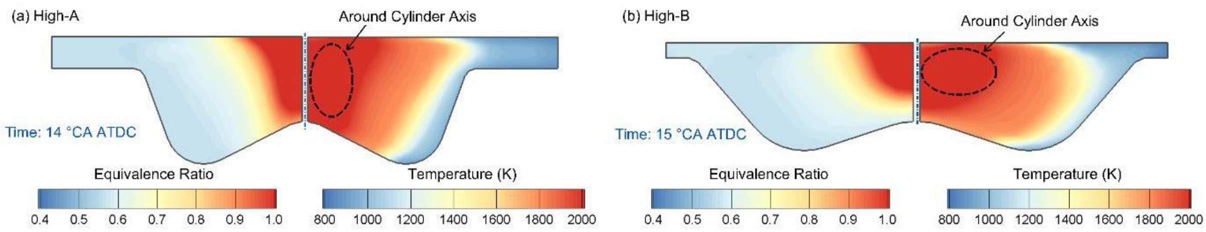


Fig. 19. In-cylinder equivalence ratio and temperature distributions at CA50 for cases High-A and High-B.

Moreover, the differences existing in the energy fraction of the heat transfer losses (see Fig. 12) between the optimal cases at each load can be further explained in this section. At low load, it is easy to find that the re-entrant type bowl of case Low-B exhibits a larger surface area compared with the open type bowl. Thus, although there is no obvious difference in the combustion temperature between cases Low-A and Low-B, the heat transfer energy fraction of case Low-B is higher than that of case Low-A due to the larger heat transfer area. Similarly, at mid load, the deep re-entrant piston bowl of case Mid-B yields a larger heat transfer surface. Meanwhile, for case Mid-B, the high-temperature region is closer to the bowl surface. Therefore, the heat transfer energy fraction is higher for case Mid-B than case Mid-A. At high load, as mentioned above, the high-temperature regions are away from the bowl surface for both the two optimal cases. This is beneficial for reducing heat transfer losses. Moreover, although the two optimal cases at high load employ the open type piston bowl, the heat transfer surface area of case High-B is smaller due to the opener and wider bowl geometry. Thus, the heat transfer energy fraction of case High-B is slightly higher than that of case High-A (see Fig. 12).

## 3.3. Correlation analysis

From the above discussion, it can be summarized that the in-cylinder fuel/air mixture formation and combustion processes are affected by the piston bowl geometry and the fuel injection strategy simultaneously. Thus, the performance of the DMDF combustion mode directly depends on the combined effects of the geometric parameters and the fuel injection parameters. For further understanding the influences of these parameters on the DMDF combustion mode, a correlation analysis was conducted to investigate the sensitivity of the engine performance to the various parameters at each load in this section. It is noted that 14 parameters were considered as the optimization variables in this study, which results in the significant complexity of the correlation analysis. Fortunately, a large number of cases (*i.e.*, citizens) were generated in the GA calculation process. In addition, with the introduction of the Sobol sequence sampling method for GA in this study, the distribution uniformity for the multi-dimensional variables of the numerous cases can be ensured, which provides a high-quality database for the correlation analysis in this section. The aim of the correlation analysis is to investigate the influence weight of each input parameter to the performance parameter including emissions for the DMDF concept.

Before the correlation analysis, the seven geometric parameters (see Fig. 3) were cut down and transferred into four key parameters for simplifying the analysis complexity. Fig. 20 depicts the definitions of the four new geometric parameters, including Depth1, Depth2, Width, and Open Extent (OE). The variable of Width is defined as the distance from the cylinder axis to the right edge of the piston bowl. Moreover, as indicated in Fig. 1, the piston bowl profile consists of two lines and three circle curves. The type of the piston bowl is directly determined by the orientation of Line2. Thus, in this section, a new parameter, *i.e.*, Open Extent, is introduced to describe the piston bowl type. The definition of Open Extent can be found in Fig. 20, which is equal to the ratio of R1 to R2 where R1 and R2 are the distances from the cylinder axis to the endpoints of Line2. Overall, the four new geometric parameters can well reflect the piston bowl characteristics.

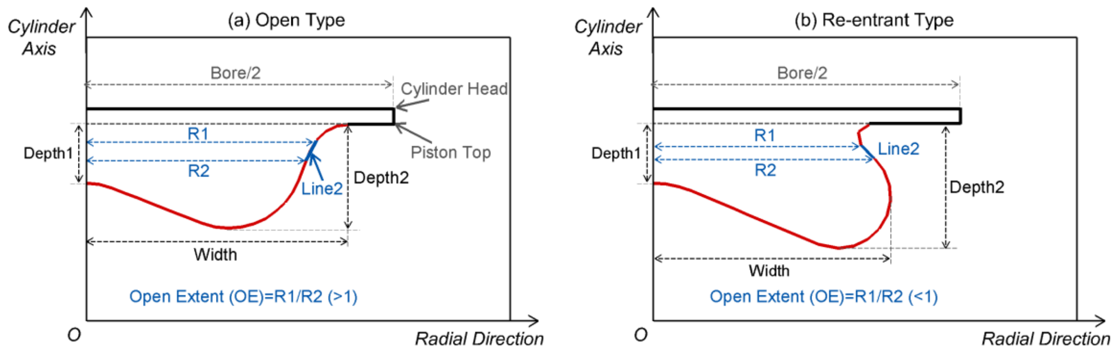


Fig. 20. Illustration of the key parameters for describing the bowl geometry of different types.

Subsequently, the correlation analysis was conducted between the input parameters and the performance parameters. The input parameters contain the four new geometric parameters and five injection parameters, including the SOI1, SOI2, MF1, SA, and $p_{inj}$. The performance parameters contain the energy fractions of heat transfer losses (HTL) and combustion losses (CL), as well as the $NO_x$ and soot emissions, which can reflect the combustion and emission characteristics of the DMDF engine. In this study, the correlation analysis is performed based on the Spearman Rank Correlation (SRC) coefficient [46]. This method is capable of providing the statistical relevance between the model input parameters and the target output parameters, and it has been widely used in engineering applications [47-49]. The SRC coefficient is defined as

$$\mathrm{SRC} = \frac{\mathrm{COV}(R_x, R_y)}{\sigma_{R_x}\sigma_{R_y}} \tag{1}$$

where *x* and *y* respectively represent the input and target output parameters, $R_x$ and $R_y$ respectively denote the rank values of parameters *x* and *y*, $\mathrm{COV}(R_x, R_y)$ is the covariance of $R_x$ and $R_y$, and $\sigma_{Rx}$ and $\sigma_{Ry}$ represent the standard deviations of $R_x$ and $R_y$. In this study, the samples are chosen from the citizens generated in the GA calculation. After excluding the unreasonable cases with deteriorated combustion efficiency or rough engine operations, around 500 effective cases are retained as the samples for the correlation analysis at each load.

Figs. 21 to 23 illustrate the SRC coefficient of each input parameter to each performance parameter at low, mid, and high loads, respectively. In each figure, the left and right parts depict the SRC coefficient of the geometric parameters and the injection parameters, respectively. The range of the SRC coefficient is from −1.0 to 1.0. The impact of the input parameters on the performance parameters or the sensitivity of the performance parameters to the input parameters can be quantitatively described by the absolute value of the SRC coefficient. Furthermore, as shown in Figs. 21 to 23, the sum of the SRC coefficient can reflect the total contributions of the geometric or injection parameters to a single performance parameter.

As illustrated in Fig. 21, at low load, for $NO_x$ and soot emissions, the effects of the injection parameters are more significant compared to the geometric parameters. On the contrary, for heat transfer losses (HTL), the geometric parameters exert more obvious influences. As for the combustion losses (CL), the effects of the geometric parameters are equivalent to those of the injection parameters. At mid load, it is seen from Fig. 22 the sensitivity of the soot emissions and HTL to the input parameters increases, especially for the geometric parameters. For the $NO_x$ emissions and CL, the injection parameters still play more important roles in contrast to the geometric parameters. At high load, it is seen from Fig. 23 the sensitivity of the performance parameters to the injection parameters increase globally. The total SRC coefficients of the geometric parameters for the performance parameters are all lower than those of the injection parameters, except for HTL. This indicates that the fuel injection event becomes more crucial for managing the engine performance as load increases. Over the whole load range, among the injection parameters, the fuel injection timings and injection pressure contribute more significant influence to the performance parameters.

Overall, from the comparison results of Figs. 21 to 23, the sensitivity of the performance parameters at different loads can be summarized. For HTL, the geometric parameters contribute more significant effects than the injection parameters for all loads, although the sensitivity to the injection parameters is increased with at higher load. For CL, the effects of the geometric parameters are equivalent to those of the injection parameters at low load. With load increasing, the sensitivity of CL to the geometric parameters decreases, whereas the injection parameters still contribute obvious influences to the CL at mid and high loads. In terms of the emissions, the $NO_x$ emissions are more sensitive to the injection parameters than the geometric parameters over the whole load range. As for the soot emissions, the influences of both the injection and geometric parameters become more significant as load increases. Thus, it can be summarized that for HTL, CL, and soot emissions, the sensitivity to the injection parameters is lower at low load and is higher at mid and high loads. For the $NO_x$ emissions, the sensitivity to the injection parameters is lower at low and mid loads. By contrast, at high load, the sensitivity of the $NO_x$ emissions to the injection parameters is relatively higher. Overall, it can be concluded that the fuel injection event becomes more important for managing the engine performance and emissions as load increases

Moreover, the key individual input parameters with crucial influences on the performance parameter can be further summarized as well. Among the geometric parameters, the most influential parameters are Width and Open Extent (OE), which is also indicated in Ref. [44]. In particular, the two parameters exert obvious and consistent impacts on heat transfer losses over the whole load range. It is indicated from Figs. 21 to 23 that the heat transfer losses can be reduced with a wider and more open piston bowl. As for the injection parameters, the fuel injection timings (*i.e.*, SOI1 and SOI2) and injection pressure (*i.e.*, $p_{inj}$) contribute more influences on the engine performance in contrast to other parameters when load increases.

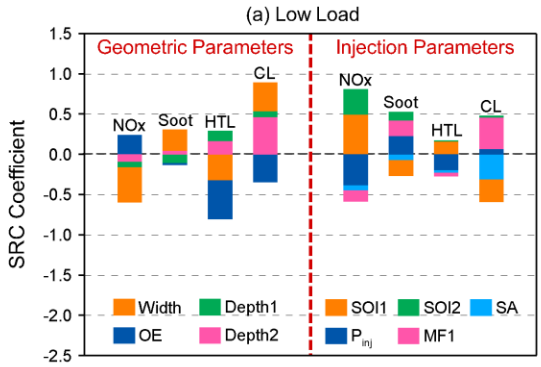


Fig. 21. SRC coefficient of each input parameter for each performance parameter at low load.

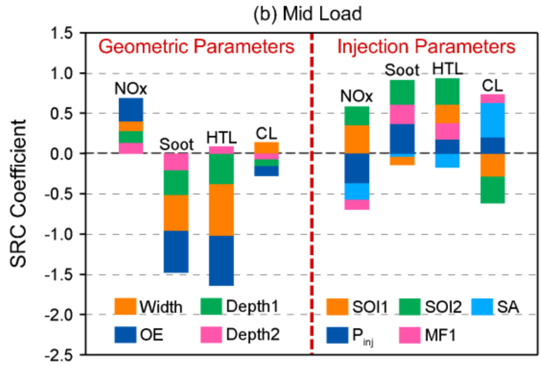


Fig. 22. SRC coefficient of each input parameter for each performance parameter at mid load.

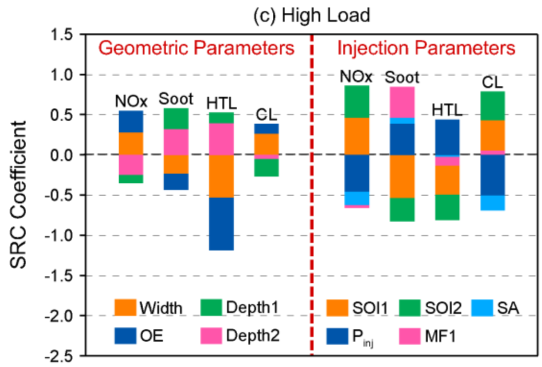


Fig. 23. SRC coefficient of each input parameter for each performance parameter at high load.

# 4. Conclusions

Based on the DMDF combustion mode, the combined optimization of the piston bowl geometry and the fuel injection strategy was performed over a wide load range using an improved genetic algorithm coupled with the CFD simulation in this work. The optimal piston bowl shape coupled with the desired injection strategy at different loads was summarized, and the improvements of engine performance were analyzed compared with the previous results about the DMDF studies. Furthermore, a correlation analysis was conducted to investigate the sensitivity of engine performance to the geometric parameters and the injection parameters. The major conclusions can be summarized as follows.

1. By optimizing the piston bowl geometry coupled with the injection strategy, the behavior of the DMDF combustion mode is further enhanced at various loads. Over the test load range, the thermal efficiency is increased up to 1.4%, 4.4%, and 1.4% for the low, mid, and high loads, respectively. An indicated thermal efficiency up to 51.8% can be realized at mid load with the combined optimization. Meanwhile, for all the optimal cases, the $NO_x$ and soot emissions can meet the Euro VI limits.
2. The optimal piston bowl shape integrated with the corresponding injection strategy is summarized at each load, providing guidelines for the piston structure design. At low load, both of the re-entrant and open type piston bowl can be equipped. At mid load, the shallow open piston bowl and the deep re-entrant piston bowl can be utilized. At high load, the open type piston bowl is preferred. The combustion occurrence location is determined by the combined effect of the piston bowl geometry and the injection strategy. Overall, the re-entrant type or deep piston bowls are good at organizing strong in-cylinder flow, which is beneficial for the fuel/air mixing.
3. The fuel injection event becomes more important for managing the engine performance and emissions as load increases. Among the injection parameters, fuel injection timings (*i.e.*, SOI1 and SOI2) and injection pressure (*i.e.*, $p_{inj}$) contribute more influences on the engine performance and emissions.
4. The piston bowl geometric parameters contribute more significant effects on the heat transfer losses than the injection parameters for all loads, although the sensitivity to the injection parameters is increased with the higher

load. Among the geometric parameters, the most influential parameters are Width and Open Extent (OE). The heat transfer losses can be reduced with a wider and more open piston bowl.

The future research work will be focused on applying the numerical optimization results in practical engine experiments. The optimized piston bowl shapes at different loads are will also be integrated into one general shape for simultaneously considering engine performance and emissions at various operating conditions.

## Acknowledgments

This work was partially supported by the National Natural Science Foundation of China (Grant Nos. 51961135105 and 91641117) and Postdoctoral Research Foundation of China (Grant Nos. 2019M661094 and 2020T130075). The experimental results used in this investigation were obtained in a project funded by VOLVO Group Trucks Technology. The authors also acknowledge FEDER and Spanish Ministerio de Economía y Competitividad for partially supporting this research through TRANCO project (TRA2017-87694-R) and the Universitat Politècnica de València for partially supporting this research through Convocatoria de ayudas a Primeros Proyectos de Investigación (PAID-06-18).

# References


[1] Johnson TV. Diesel emission control in review. SAE Technical Paper; 2009; no. 2009-01-0121.

[2] Musculus MP, Miles PC, Pickett LM. Conceptual models for partially premixed low-temperature diesel combustion. Prog Energy Combust Sci. 2013;39(2):246-83.

[3] Reitz RD, Duraisamy G. Review of high efficiency and clean reactivity controlled compression ignition (RCCI) combustion in internal combustion engines. Prog Energy Combust Sci. 2015;46:12-71.

[4] Benajes J, García A, Pastor JM, Monsalve-Serrano J. Effects of piston bowl geometry on reactivity controlled compression ignition heat transfer and combustion losses at different engine loads. Energy. 2016;98:64-77.

[5] Li Y, Jia M, Chang Y, Kokjohn SL, Reitz RD. Thermodynamic energy and exergy analysis of three different engine combustion regimes. Appl Energy. 2016;180:849-58.

[6] Gong C, Li Z, Yi L, Liu F. Comparative study on combustion and emissions between methanol port-injection engine and methanol direct-injection engine with $H_2$-enriched port-injection under lean-burn conditions. Energy Convers Manage. 2019;200:112096.

[7] Tong L, Wang H, Zheng Z, Reitz R, Yao M. Experimental study of RCCI combustion and load extension in a compression ignition engine fueled with gasoline and pode. Fuel. 2016;181:878-86.

[8] Lim JH, Reitz RD. High load (21 bar IMEP) dual fuel RCCI combustion using dual direct injection. J Eng Gas Turbines Power. 2014;136(10):101514(1-10).

[9] Wang Y, Yao M, Li T, Zhang W, Zheng Z. A parametric study for enabling reactivity controlled compression ignition (RCCI) operation in diesel engines at various engine loads. Appl Energy. 2016;175:389-402.

[10] Molina S, García A, Pastor JM, Belarte E, Balloul I. Operating range extension of RCCI combustion concept from low to full load in a heavy-duty engine. Appl Energy. 2015;143:211-27.

[11] Xu G, Jia M, Li Y, Chang Y, Wang T. Potential of reactivity controlled compression ignition (RCCI) combustion coupled with variable valve timing (VVT) strategy for meeting Euro 6 emission regulations and high fuel efficiency in a heavy-duty diesel engine. Energy Convers Manage. 2018;171:683-98.

[12] Xu GF, Jia M, Li YP, Chang YC, Liu H, Wang TY. Evaluation of variable compression ratio (VCR) and variable valve timing (VVT) strategies in a heavy-duty diesel engine with reactivity controlled compression ignition (RCCI) combustion under a wide load range. Fuel. 2019;253:114-28.

[13] Mikulski M, Balakrishnan PR, Doosje E, Bekdemir C. Variable valve actuation strategies for better efficiency load range and thermal management in an RCCI engine. SAE Technical Paper; 2018; no. 2018-01-0254.

[14] Benajes J, Pastor JV, García A, Boronat V. A RCCI operational limits assessment in a medium duty compression ignition engine using an adapted compression ratio. Energy Convers Manage. 2016;126:497-508.

[15] Benajes J, García A, Monsalve-Serrano J, Boronat V. Achieving clean and efficient engine operation up to full load by combining optimized RCCI and dual-fuel diesel-gasoline combustion strategies. Energy Convers Manage. 2017;136:142-51.

[16] Benajes J, García A, Monsalve-Serrano J, Lago Sari R. Fuel consumption and engine-out emissions estimations of a light-duty engine running in dual-mode RCCI/CDC with different fuels and driving cycles. Energy. 2018;157:19-30.

[17] García A, Monsalve-Serrano J, Villalta D, Sari R. Fuel sensitivity effects on dual-mode dual-fuel combustion operation for different octane numbers. Energy Convers Manage. 2019;201:112137.

[18] Macián V, Bermúdez V, Villalta D, Soto L. Effects of low-pressure EGR on gaseous emissions and particle size distribution from a dual-mode dual-fuel (DMDF) concept in a medium-duty engine. Appl Therm Eng.

2019;163:114245.

[19] Xu G, Monsalve-Serrano J, Jia M, García A. Computational optimization of the dual-mode dual-fuel concept through genetic algorithm at different engine loads. Energy Convers Manage. 2020;208:112577.

[20] García A, Gil A, Monsalve-Serrano J, Lago Sari R. OMEx-diesel blends as high reactivity fuel for ultra-low NOx and soot emissions in the dual-mode dual-fuel combustion strategy. Fuel. 2020;275:117898.

[21] García A, Monsalve-Serrano J, José Sanchís E, Fogué-Robles Á. Exploration of suitable injector configuration for dual-mode dual-fuel engine with diesel and OMEx as high reactivity fuels. Fuel. 2020;280:118670.

[22] Dempsey AB, Walker NR, Reitz RD. Effect of piston bowl geometry on dual fuel reactivity controlled compression ignition (RCCI) in a light-duty engine operated with gasoline/diesel and methanol/diesel. SAE Technical Paper; 2013; no. 2013-01-0264.

[23] Park SW. Optimization of combustion chamber geometry for stoichiometric diesel combustion using a micro genetic algorithm. Fuel Process Technol. 2010;91(11):1742-52.

[24] Xu L, Bai X-S, Li Y, Treacy M, Li C, Tunestål P, Tunér M, Lu X. Effect of piston bowl geometry and compression ratio on in-cylinder combustion and engine performance in a gasoline direct-injection compression ignition engine under different injection conditions. Appl Energy. 2020;280:115920.

[25] Nazemian M, Neshat E, Saray RK. Effects of piston geometry and injection strategy on the capacity improvement of waste heat recovery from RCCI engines utilizing DOE method. Appl Therm Eng. 2019;152:52-66.

[26] Lee S, Park S. Optimization of the piston bowl geometry and the operating conditions of a gasoline-diesel dual-fuel engine based on a compression ignition engine. Energy. 2017;121:433-48.

[27] Badra J, khaled F, Sim J, Pei Y, Viollet Y, Pal P, Futterer C, Brenner M, Som S, Farooq A, Chang J.

Combustion system optimization of a light-duty GCI engine using cfd and machine learning. SAE Technical Paper; 2020; no. 2020-01-1313.

[28] Amsden AA. KIVA-3V: A block structured KIVA program for engines with vertical and canted valves. USA: Los Alamos National Laboratory Technical Report; 1997. LA-13313-MS.

[29] Wang BL, Lee CW, Reitz RD, Miles PC, Han Z. A generalized renormalization group turbulence model and its application to a light-duty diesel engine operating in a low-temperature combustion regime. Int J Engine Res. 2012;14(3):279-92.

[30] Zhang Y, Jia M, Liu H, Xie M, Wang T, Zhou L. Development of a new spray/wall interaction model for diesel spray under PCCI-engine relevant conditions. Atomization and Sprays. 2014;24(1):41-80.

[31] Zhang Y, Jia M, Liu H, Xie M. Development of an improved liquid film model for spray/wall interaction under engine-relevant conditions. Int J Multiphase Flow. 2016;79:74-87.

[32] Yi P, Long W, Jia M, Tian J, Li B. Development of a quasi-dimensional vaporization model for multi-component fuels focusing on forced convection and high temperature conditions. Int J Heat Mass Transfer. 2016;97:130-45.

[33] Zhang Y, Jia M, Yi P, Liu H, Xie M. An efficient liquid film vaporization model for multi-component fuels considering thermal and mass diffusions. Appl Therm Eng. 2017;112:534-48.

[34] Cao J, Jia M, Niu B, Chang Y, Xu Z, Liu H. Establishment of an improved heat transfer model based on an enhanced thermal wall function for internal combustion engines operated under different combustion modes. Energy Convers Manage. 2019;195:748-59.

[35] Nordin PAN. Complex chemistry modeling of diesel spray combustion. Sweden: Chalmers University of Technology; 2001. PhD Thesis.

[36] Ricart LM, Reltz RD, Dec JE. Comparisons of diesel spray liquid penetration and vapor fuel distributions

with in-cylinder optical measurements. J Eng Gas Turbines Power. 2000;122(4):588-95.

[37] Kee RJ, Rupley FM, Meeks E, Miller JA. Chemkin-III: A fortran chemical kinetics package for the analysis of gas phase chemical and plasma kinetics. USA: Sandia National Laboratory Technical Report; 1996. SAND96-8216.

[38] Chang Y, Jia M, Li Y, Xie M. Application of the optimized decoupling methodology for the construction of a skeletal primary reference fuel mechanism focusing on engine-relevant conditions. Front Mech Eng. 2015;1:1-11.

[39] Xu G, Jia M, Li Y, Chang Y, Liu H, Wang T. Evaluation of variable compression ratio (VCR) and variable valve timing (VVT) strategies in a heavy-duty diesel engine with reactivity controlled compression ignition (RCCI) combustion under a wide load range. Fuel. 2019;253:114-28.

[40] Li Y, Jia M, Chang Y, Xu Z, Xu G, Liu H, Wang T. Principle of determining the optimal operating parameters based on fuel properties and initial conditions for RCCI engines. Fuel. 2018;216:284-95.

[41] Kim M, Reitz RD, Kong SC. Modeling early injection processes in hsdi diesel engines. SAE Technical Paper; 2006; no. 2006-01-0056.

[42] Deb K, Pratap A, Agarwal S, Meyarivan T. A fast and elitist multiobjective genetic algorithm: NSGA-II. IEEE Trans Evol Comput. 2002;6(2):182-97.

[43] Navid A, Khalilarya S, Abbasi M. Diesel engine optimization with multi-objective performance characteristics by non-evolutionary Nelder-Mead algorithm: Sobol sequence and latin hypercube sampling methods comparison in doe process. Fuel. 2018;228:349-67.

[44] Miles PC, Andersson Ö. A review of design considerations for light-duty diesel combustion systems. Int J Engine Res. 2015;17(1):6-15.

[45] Lee J, Lee S, Kim J, Kim D. Bowl shape design optimization for engine-out PM reduction in heavy duty

diesel engine. SAE Technical Paper; 2015; no. 2015-01-0789.

[46] Chang Y, Jia M, Niu B, Xie M, Zhou C. Reduction of detailed chemical mechanisms using reaction class-based global sensitivity and path sensitivity analyses. Energy Fuels. 2019;33(9):9289-301.

[47] Fridlyand A, Johnson MS, Goldsborough SS, West RH, McNenly MJ, Mehl M, Pitz WJ. The role of correlations in uncertainty quantification of transportation relevant fuel models. Combust Flame. 2017;180:239-49.

[48] Chang Y, Jia M, Niu B, Zhang Y, Xie M, Li Y. Construction and assessment of reduced oxidation mechanisms using global sensitivity analysis and uncertainty analysis. Proc Combust Inst. 2019;37(1):751-61.

[49] Hébrard É, Tomlin AS, Bounaceur R, Battin-Leclerc F. Determining predictive uncertainties and global sensitivities for large parameter systems: A case study for n-butane oxidation. Proc Combust Inst. 2015;35(1):607-16.